



Hydrometeor partitioning ratios for dual-frequency space-borne and polarimetric ground-based radar observations

Velibor Pejčic¹, Kamil Mroz², Kai Mühlbauer¹, and Silke Trömel^{1,3}

¹Institute of Geosciences, Department of Meteorology, University of Bonn, Bonn, Germany

²National Center for Earth Observation, University of Leicester, Leicester, UK

³Laboratory for Clouds and Precipitation Exploration, Geoverbund ABC/J, Bonn, Germany

Correspondence: Velibor Pejčic (velibor@uni-bonn.de)

Abstract. Conventional radar-based hydrometeor classification (HMC) algorithms identify the dominant hydrometeor type within a resolved radar volume, while more recent techniques allow estimation of the proportions of individual hydrometeor classes (hydrometeor partitioning ratios, HPRs) within a mixture. These newer algorithms (HMC_P^{DP}) are based on dual-polarization (DP) measurements from ground-based radars (GR), while similar algorithms do not yet exist for space-borne radars (SR) with dual-frequency (DF) capabilities. This study has three objectives, (1) to evaluate HPR retrievals, (2) to exploit the combination of DF SR and DP GR for estimating HPR based on satellite DF observations (HPR_k^{DF}) and (3) to further improve HPR_k^{DP} estimates based on GR DP observations. To achieve these, DP measurements of NEXRAD's GRs are matched with those of the dual-frequency precipitation radar of the Global Precipitation Measurement Core satellite. All matched volumes are represented by averaged DF and DP observations and several hundred GR sub-volumes classified with the standard HMC. The latter are used to calculate quasi-HPRs (qHPRs). qHPRs and averaged DF and DP variables serve as basis for the HPR_k^{DF} and HPR_k^{DP} retrievals, which in turn are evaluated with the qHPRs. The vertical distributions of HPR_k^{DF} and HMC_P^{DP} products are in good agreement. Furthermore, the estimated HPRs show for most hydrometeor classes high correlations with the qHPRs and confirm the overall good performance of the algorithms. However, HMC_P^{DP} performance is superior to HMC_P^{DF} . In both DF and DP space, snow HPRs are underestimated, graupel HPRs are overestimated, and HPRs for big drops show only low correlations.

1 Introduction

Hydrometeor classifications (HMC) using ground-based polarimetric weather radars (GR) observations play an essential role, e.g. to refine quantitative precipitation estimation (Giangrande and Ryzhkov, 2008), to detect hail and estimate its size and damage potential (Ortega et al., 2016; Ryzhkov et al., 2013; Ackermann et al., 2023) and to identify freezing rain (Thompson et al., 2014), which can serve as a warning system for transport infrastructure (Trömel et al., 2017). The majority of HMCs identify the dominant hydrometeor type within each resolved radar volume exploiting measurements from dual-polarization (DP) weather radars and specific classification methods. The most commonly used classification methods are based on the fuzzy logic approach (Dolan and Rutledge, 2009; Dolan et al., 2013; Zrníć et al., 2001a; Straka et al., 2000; Thompson et al., 2014; Ribaud et al., 2016; Park et al., 2009), but there are also methods that rely on the Bayesian approach (Yang et al., 2019;



25 Marzano et al., 2007) or clustering techniques (Grazioli et al., 2015; Ribaud et al., 2019; Lukach et al., 2020; Besic et al., 2016). More detailed description of hydrometeor mixtures (Besic et al., 2018) are the so-called hydrometeor partitioning ratios (HPRs), which represent estimates of the proportion of the polarimetric signal originating from a specific hydrometeor class within a resolved radar volume. Besic et al. (2018) provided a methodology to estimate HPRs, which was subsequently refined in Trömel et al. (2023). HPRs have recently been utilized to study microphysics and dynamics of precipitation (Gehring et al., 30 2020, 2022), to verify microphysical retrievals (Billault-Roux et al., 2023; Planat et al., 2021) and to evaluate hydrometeor distributions in NWP models (Trömel et al., 2021; Vignon et al., 2019; Jang et al., 2021; Shrestha et al., 2022; Trömel et al., 2023).

Only a few space-borne measurement platforms with radars exist or have existed in the past: CloudSat (Stephens et al., 2002), designed for observations of clouds and light precipitation, the Tropical Rainfall Measuring Mission (TRMM; Liu 35 et al., 2012), which is the first precipitation satellite with a K_u -band precipitation radar (PR) on board, and its successor the Global Precipitation Measurement core satellite (GPM) with the first Dual-Frequency Precipitation Radar (DPR) measuring precipitation at K_u -band and K_a -band frequencies (Hou et al., 2014). Rain rates estimated from space-borne radars (SR) are significantly affected by the hydrometeor types located within a resolved measurement volume (Liao and Meneghini, 2022). SR-derived HMCs, using the DPR e.g., are based on very simple subdivisions of the hydrometeors. The detection of the melting 40 layer (ML) top and bottom is used to distinguish between solid, liquid and melting hydrometeors (Le et al., 2016). Additional two-dimensional classifications are provided for snow (*flagSurfaceSnowfall*; Le et al., 2017)), graupel/hail (*flagGraupelHail*; Le and Chandrasekar, 2021a) and hail (*flagHail*; Le and Chandrasekar, 2021b) and are based on the so-called precipitation type index (PTI). The PTI is derived from the storm top height (STH), the maximum measured reflectivity at K_u -band and the average slope of the dual-frequency ratio profile. Mroz et al. (2017) presented several hail detection algorithms based on 45 DF profile observations but also on brightness temperature measurements of GPMs Microwave Imager (GMI). All products do not provide information on the vertical distribution of these hydrometeor classes and are not considered in DPRs rain rates estimation (Iguchi et al., 2010). Seiki (2021) was the first to develop a three-dimensional HMC based on dual-frequency (DF) measurements, but only for hail detection.

In this study, the HMC scheme from Trömel et al. (2023) (HMC_P), estimating HPRs in DP-space (HMC_P^{DP}), is refined and 50 extended to the DF-space (HMC_P^{DF}). For this purpose, satellite-based DF observations from GPM's DPR are combined with ground-based DP measurements from NEXRAD's S-band WSR-88D radars. In order to combine the high-resolution GR and the low-resolution SR data, the DF and DP measurements are averaged to obtain data with approximately equal volumes, so-called superobbed data. Each superobbed observation then contains information about the partitioning ratios of the different dominant hydrometeor classes (quasi hydrometeor partitioning ratio, qHPR), approximated by the relative occurrences of the 55 dominant hydrometeor classes in high-resolution radar bins within the superobbed volume as determined by conventional DP-based HMC. These qHPRs are used as a basis for the derivation of the HPRs in DF and DP space. Subsequently, the HPRs estimated with HMC_P from either superobbed DF or DP measurements are validated using the qHPR estimates.



Sect. 2 introduces the SR and GR measurements and their processing, followed by the explanations of the merging procedure and the qHPR derivation. Sect. 3 explains the methodology for HPR estimates. The results are shown in Sect. 4 followed by a conclusion in Sect. 5.

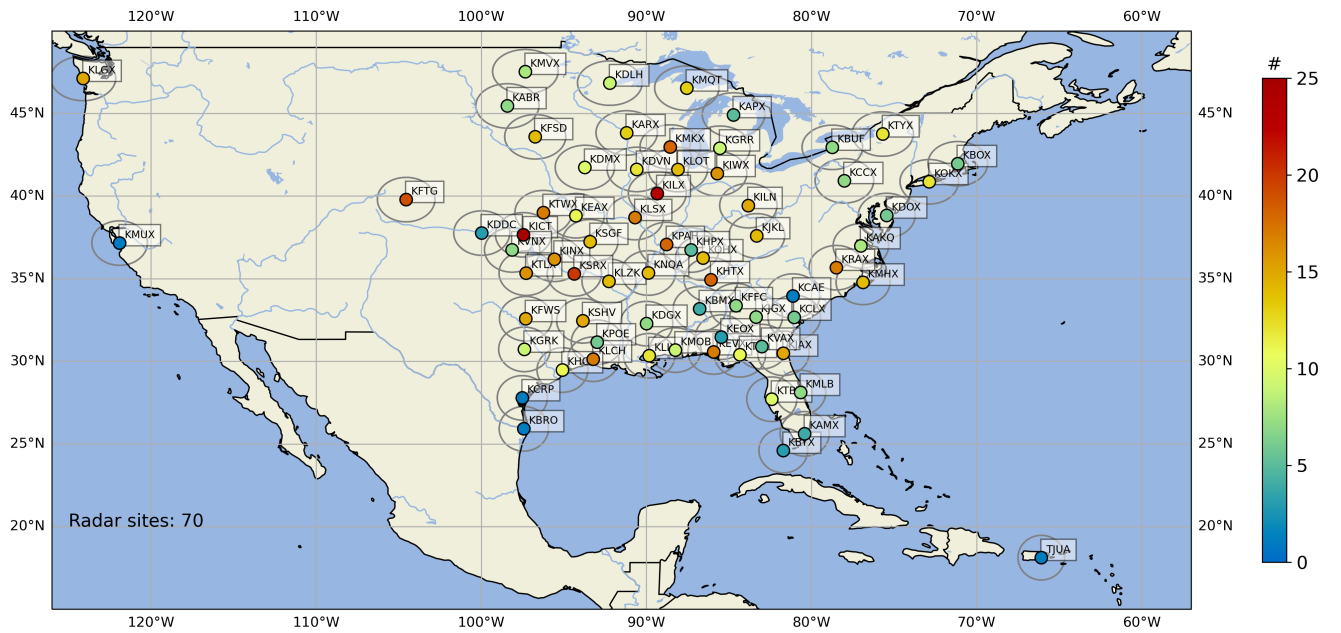


Figure 1. Overview of the NEXRAD weather radar (WSR-88D) sites used in this study. The 150 km range for an elevation angle of 0.5° is illustrated as gray circle. The colored dots indicate the location of the respective radar and the number of GPM overpasses in the period between 2014 and 2023 used in this study. The total number of used radar sites is indicated in the lower left corner.

2 Data

2.1 Space-borne radar observations

The DPR onboard the GPM Core Observatory (Iguchi and Meneghini, 2021) comprises two radars: the K_u -band Precipitation Radar (K_u PR, 13.6 GHz) and the K_a -band Precipitation Radar (K_a PR, 35.5 GHz). The DPR provides measurements with a vertical resolution of 250 m, over-sampled every 125 m, and a horizontal resolution of approximately 5 km due to the satellite's altitude of 407 km before the orbit boost in November 2024 (Kubota et al., 2024).



Initially, the K_u PR operated across a 245 km wide swath (49 beams), while the K_a PR was limited to a narrower central swath of 125 km (25 beams), nested within the K_u PR swath. The K_a PR employed two distinct scanning modes: Measurements with a vertical resolution of 250 m, fully overlapping the central part of the K_u PR swath (High-Resolution Mode).
70 Measurements with a vertical resolution of 500 m, where the scan pattern was laterally shifted by half a footprint (24 beams) in the cross-track direction (Shifted Scan Mode, Hou et al., 2014).

On 21 May 2018, the scanning strategy was updated to extend the K_a PR swath to 245 km, matching the K_u PR swath width. The 24 beams were moved to the outer parts of the swath. This adjustment ensured that all footprints in the extended K_a PR swath included DF measurements, significantly enhancing data consistency and coverage (Iguchi et al., 2010). Single-
75 frequency beams are not considered in this study. To derive parameters of the drop size distribution (DSD), precipitation rates and attenuation corrected K_u -band and K_a -band reflectivities in logarithmic space, the measured K_a -band ($Z_{K_a}^m$) and K_u -band ($Z_{K_u}^m$) reflectivities are processed in various modules described in more detail in Iguchi et al. (2010). The DF ratio

$$DFR_{K_u-K_a}^m = Z_{K_u}^m - Z_{K_a}^m \quad (1)$$

is the difference between $Z_{K_u}^m$ and $Z_{K_a}^m$ reflectivities in logarithmic space. In stratiform precipitation $DFR_{K_u-K_a}^m$ is mainly
80 affected by non-Rayleigh scattering effects and path-integrated attenuation. In the solid phase, attenuation by frozen hydrometeors is negligible for both frequencies and does not significantly change $DFR_{K_u-K_a}^m$. In contrast, the non-Rayleigh scattering effects play a major role and lead to an increase of the $DFR_{K_u-K_a}^m$ with increasing hydrometeor diameters (Le et al., 2016; Iguchi et al., 2018). Also, $DFR_{K_u-K_a}^m$ in the solid region depends on the density of hydrometeors and their degree of riming. According to the Mie theory an increase in $DFR_{K_u-K_a}^m$ is expected with decreasing density of fluffy non-rimed solid hydrometeors with low $Z_{K_u}^m$ (Seiki, 2021). For a fixed $DFR_{K_u-K_a}^m$ $Z_{K_u}^m$ increases with the ice particles degree of riming. However, this
85 is only valid in stratiform precipitation and if $DFR_{K_u-K_a}^m > 1$ dB (Tridon et al., 2019). In the melting layer (ML) we observe an increase in $Z_{K_u}^m$ due to the changes in the refractive index, particle size and concentration (Ryzhkov and Zrnica, 2019). As a consequence, both non-Rayleigh scattering effects and attenuation increase the $DFR_{K_u-K_a}^m$ and result in a pronounced "bump", called the $DFR_{K_u-K_a}^m$ bright band, in the vertical profile of the $DFR_{K_u-K_a}^m$ (Le et al., 2016). In the liquid phase, attenuation
90 mainly controls the $DFR_{K_u-K_a}^m$. K_a -band measurements are much more affected by attenuation compared to measurements at K_u -band and lead to an increase in $DFR_{K_u-K_a}^m$ towards the ground. This increase is even more pronounced in convective precipitation where higher precipitation rates, thus the attenuation values, are observed. Furthermore, convection promotes the presence of large hydrometeors such as graupel, hail or drop diameter exceeding 0.8 mm (Mroz et al., 2024) that contribute to non-Rayleigh related $DFR_{K_u-K_a}^m$ increase. In deep convective cores, the typical vertical profile of $DFR_{K_u-K_a}^m$ can be dis-
95 torted by multiple scattering at K_a -band. In extreme MS conditions, attenuation of the high frequency radar observations is compensated by multiple scattering effects in the upper part of the atmosphere which results in the so-called $DFR_{K_u-K_a}^m$ -knee, i.e. a decrease in $DFR_{K_u-K_a}^m$ towards the ground (Battaglia et al., 2014).

The overall vertical structure of the $DFR_{K_u-K_a}^m$ is used to categorize the measurements into different rain types (stratiform, convective, other, see Le et al. (2016)) and to determine the ML thickness and height, and is used to distinguish between liquid,
100 solid and melting precipitation regions (Iguchi et al., 2010; Le and Chandrasekar, 2012).

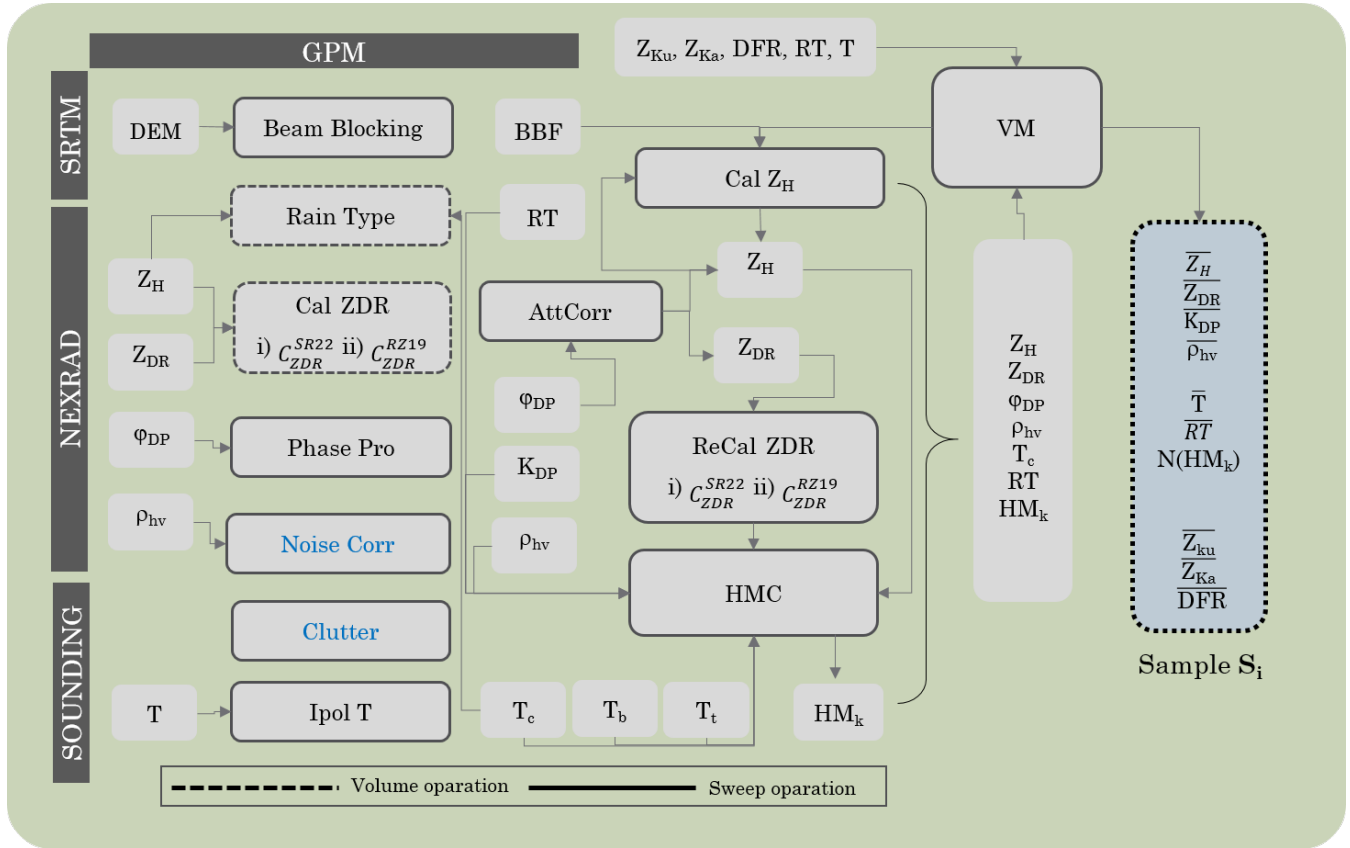


Figure 2. Workflow for polarimetric radar data processing of the NEXRAD S-band weather radars (gray boxes). The black boxes represent the different data sources used and the gray boxes outlined with solid or dashed lines represent processing operations based on a sweep or volume data, respectively. Operations that have already been performed on the NEXRAD data are written in blue.

2.2 Ground-based radar observations

DP measurements of the NEXRAD WSR-88D S-band weather radars are exploited for this study. In total, 757 volume scans measured between 2014 and 2023 of the radar sites shown in Fig. 1 are considered. Measurements were selected to ensure that the GPM overflight took place at the closest point in time. A balanced number of convective and stratiform events is maintained to ensure a good representation of less frequently occurring hydrometeors like hail. The range resolution of the utilized NEXRAD radars is 250 m with a maximum elevation angle of 19.5° and 1° degree azimuthal resolution for higher elevation. Quality-controlled GR observations are provided by NASA's GPM Ground Validation program (GPM-GV). The quality control includes non-precipitating echos removal with different thresholds and phase unfolding. In addition, GPM-GV also provides vertical temperature information from model soundings (Pippitt et al., 2013). Additional GR processing (Fig. 2) is explained in more detail in the following:



The vertical temperature profiles are interpolated linearly at the beam center (T_c) and at the respective outer beam edges (3 dB beam width). From now on referred to T_t as temperature at the top beam edge and T_b as the temperature at the bottom beam edge. All radar bins with $T_b < 0^\circ\text{C}$ are classified as solid and all those with $T_t > 4^\circ\text{C}$ as liquid. All other radar measurements are considered as partly melted. Digital Elevation Model (DEM) data from the Shuttle Radar Topography Mission (SRTM, Reuter et al. (2007)) is used to calculate any possible beam blocking fractions (BBF) following Bech et al. (2003). Z_H is smoothed with a moving average of 5 range bins, while 11 range bins are used to smooth Z_{DR} and ρ_{HV} . A ρ_{HV} threshold of 0.8 is applied for the noise filtering. In the next step, the rain type classification following Park et al. (2009) is applied to the entire volume to classify convective and stratiform radar bins, but with slight modifications (i.e., the classification as convective based on ρ_{HV} only is omitted).

For Z_{DR} calibration, either the method using Quasi-Vertical-Profiles (Sanchez-Rivas and Rico-Ramirez, 2022) in the following referred to $\text{Cal}_{Z_{DR}}^{\text{SR22}}$ or the Z_H - Z_{DR} consistency in light rain (Ryzhkov and Zrnica, 2019), referred as $\text{Cal}_{Z_{DR}}^{\text{RZ19}}$, is applied. Since the data base is limited to volume scans for specific time steps only, $\text{Cal}_{Z_{DR}}^{\text{SR22}}$ is not applied to Quasi-Vertical-Profiles but to all available PPI scans to include a larger amount of data in the calibration routine. Slight modifications of $\text{Cal}_{Z_{DR}}^{\text{SR22}}$ include the application of the median instead of the mean (Eq. 10; Sanchez-Rivas and Rico-Ramirez, 2022) for noise filtering and recalculation of the intrinsic mean Z_{DR} (0.178 dB) for the S-band data. A first guess Z_{DR} -offset, using either $\text{Cal}_{Z_{DR}}^{\text{SR22}}$ or $\text{Cal}_{Z_{DR}}^{\text{RZ19}}$ if there are less than 1000 valid radar bins, is applied on the entire volume scan before the final recalculated Z_{DR} -offset is applied after correction for (differential) attenuation sweep-wise. Valid observations for the Z_{DR} -offset calibration are all radar bins with $\rho_{HV} > 0.99$, $T_t > 5^\circ\text{C}$ and if applying $\text{Cal}_{Z_{DR}}^{\text{SR22}}$ $0 \text{ dBZ} \leq Z_H \leq 20 \text{ dBZ}$ otherwise $20 \text{ dBZ} \leq Z_H \leq 30 \text{ dBZ}$ for $\text{Cal}_{Z_{DR}}^{\text{RZ19}}$.

The processing of differential Phase ϕ_{DP} includes radial smoothing with a window size of 9 radar bins for measurements $Z_H > 40 \text{ dBZ}$ (heavy rain) and a window size of 25 radar bins elsewhere (Park et al., 2009). Instead of determining K_{DP} based on the slope of a least squares fit, a low-noise Lanczos differentiator (Heistermann et al., 2013; Diekema and Koornwinder, 2012) is used to speed up the processing significantly. The two window sizes are also applied for the K_{DP} derivation. Correction for (differential) attenuation applies parameters $\alpha = 0.04 \text{ dB deg}^{-1}$ and $\beta = 0.004 \text{ dB deg}^{-1}$ (Ryzhkov and Zrnica, 1995). The attenuation correction is limited to the liquid phase ($T_t > 4^\circ\text{C}$) and the highest values of the path-integrated attenuation (PIA) and path-integrated differential attenuation (PIDA) reached in the liquid phase are applied to the remaining mixed phase and solid radar observations.

Z_H calibration (Cal_{Z_H}) is performed by comparing the GR with SR measurements (Pejic et al., 2022; Crisologo and Heistermann, 2020; Warren et al., 2018; Louf and Protat, 2023; Protat et al., 2022). GR and SR measurements are matched to the same geometry for each volume scan (more detailed description in Sect. 2.3), but measurements contaminated by the ML are excluded from the offset calculations (Pejic et al., 2022). For this purpose, the ML top and bottom estimates determined by the DPR are used. The conversion of reflectivity from K_u -band to S-band wavelengths is performed following Cao et al. (2013). Further refinements of Cal_{Z_H} include the use of quality indices, determined from BBF and PIA, as weighting factors for determining the Z_H -offset (Crisologo and Heistermann, 2020).



145 The applied standard HMC (HMC_Z Zrnić et al., 2001b) to identify the dominant hydrometeor type in a resolved radar volume and used to estimate the qHPRs is based on two dimensional membership functions (MSF) defined in Park et al. (2009) with slightly modified hydrometeor types and MSF-parameters. The predefined hydrometeor types are light rain (LR), moderate rain (MR), heavy rain (HR), big drops (BD), rain/hail (RH), graupel (GP), crystals (IC), dry snow (SN), wet snow (WS), plates/dendrites (PD) and hail (HA). The hydrometeor classes are generally abbreviated to HM_k where $k = 1, \dots, n$ with
150 $n=11$. For more information on HMC_Z , we refer to the appendix A .

2.3 GR-SR Merging

The volume matching method (VMM) is performed with ω radlib (Heistermann et al., 2013) and represents a well-known method for transferring SR and GR measurements to comparably sized volumes. In a first step all DP measurements of all GR bins within the SR footprint are averaged (\overline{DP} , Fig. 3, left, plan view). Secondly, the DF observations of all SR bins (vertical
155 resolution 125 m) within the GR beamwidth are averaged (\overline{DF} , Fig. 3, right, side view). For more details see Warren et al. (2018) or Pejčic et al. (2022). This results in equally sized superobbed volumes described by averaged DP variables \overline{Z}_H , \overline{Z}_{DR} , \overline{K}_{DP} and $\overline{\rho}_{HV}$ and averaged DF variables $\overline{Z}_{K_u}^m$, $\overline{Z}_{K_a}^m$ and $\overline{DFR}_{K_u-K_a}^m$, from now on called sample S_i (Fig. 3, top center and Fig. 2, blue box). Furthermore, each S_i contains a mean temperature (\overline{T}) and a rain type index (\overline{RT}). \overline{RT} is convective if more than 10% of the GR pixels in a S_i are defined as convective ($\overline{RT} = 2$), otherwise \overline{RT} is defined as stratiform ($\overline{RT} = 1$). S_i also
160 includes the number of dominant hydrometeor classes $N(HM_k)$ classified with HMC_Z on the original GR radar grid (Fig. 2, blue box). For each S_i the $N(HM_k)$ are used to calculate the qHPR_k via

$$qHPR_k = \frac{N(HM_k)}{\sum_{k=0}^n N(HM_k)}. \quad (2)$$

Note that qHPRs only represent estimators for the HPRs. E.g., due to their disproportionate influence on the polarimetric moments, hail or graupel may be classified as the dominant hydrometeor class in radar volumes despite low HPR. This can lead
165 to overestimated qHPR for graupel and hail. In this study only S_i with at least 50 valid GR pixels, well-defined stratiform or convective SR profiles and DPR detected precipitation (*flagPrecip*) are considered. S_i showing strong differential attenuation due to hot spots above the ML or depolarization streaks (Ryzhkov and Zrnić, 2019) leading to negative Z_{DR} stripes are excluded. Furthermore, SR observations below 15.5 dBZ at K_u -band (Liao and Meneghini, 2022) and 18 dBZ at K_a -band (Mroz et al., 2024) are not considered.

170 80% of the S_i , including \overline{DF} , \overline{DP} measurements and qHPRs, serve as training data for the HMC_P (Fig. 3, center) and the remaining 20% of the S_i are utilized as training dataset for the evaluation. Sect. 4.1 presents results for one case study entirely independent of the test and training dataset used.

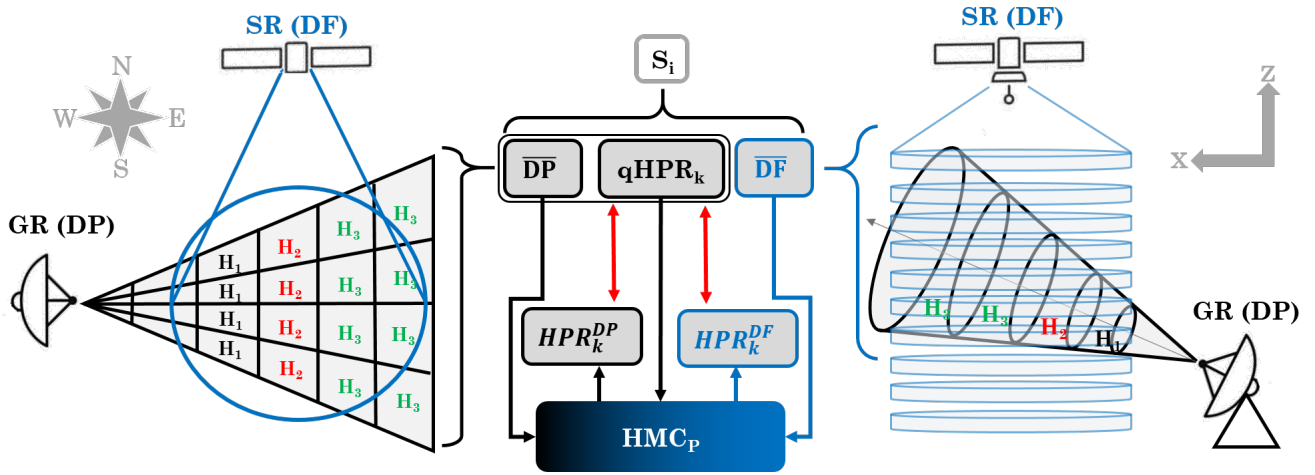


Figure 3. Schematic illustration of the workflow to derive and evaluate the HPR with HMC_P based on \overline{DF} , \overline{DP} and $qHPR_k$ (center) by comparing SR (in blue) and GR (in black) observations. The plan view on the left and the side view on the right site. The hydrometeor classes are indicated with colored H_1 , H_2 and H_3

3 Hydrometeor partitioning Ratios (HPR)

In the following, we interpret the polarimetric measurements as multidimensional vectors and thus assume HPRs can be determined based on multidimensional distribution functions p_k for the different hydrometeor classes. If the multidimensional measurement approaches the mean of a specific p_k , the HPR_k for that particular hydrometeor class k , increases, and vice versa, the farther away it is, the smaller the HPR_k becomes (Besic et al., 2018; Trömel et al., 2023). Trömel et al. (2023) introduced HMC_P as a modified version compared to Besic et al. (2018). This section details further advancements of HMC_P and additionally transfers the methodology from DP to DF observation space.

The superobbed variables in samples S_i are stored in the multidimensional observation vector

$$\mathbf{X}_i^{DP} = \begin{bmatrix} \overline{Z}_H \\ \overline{Z}_{DR} \\ \overline{K}_{DP} \\ \overline{\rho}_{HV} \\ \overline{RT} \end{bmatrix} \quad (3)$$

including the averaged DP variables \overline{Z}_H , \overline{Z}_{DR} , \overline{K}_{DP} and $\overline{\rho}_{HV}$, together with the rain type index \overline{RT} . Similarly, the multidimensional DF observation vector



$$\mathbf{X}_i^{DF} = \begin{bmatrix} \bar{Z}_{K_u}^m \\ \overline{DFR}_{K_u-K_a}^m \\ \overline{RT} \end{bmatrix} \quad (4)$$

185 includes the averaged DF variables $\bar{Z}_{K_u}^m$ and $\overline{DFR}_{K_u-K_a}^m$, together with \overline{RT} . The ensuring description of the algorithm refers to an observation vector \mathbf{X}_i and is valid for both multidimensional vectors \mathbf{X}_i^{DF} and \mathbf{X}_i^{DP} .

In order to derive p_k , weighted centroids

$$\boldsymbol{\mu}_k = \frac{\sum_{i=1}^n w_i \mathbf{X}_i}{\sum_{i=1}^n w_i} \quad (5)$$

and weighted covariance matrices

$$190 \quad \mathbf{C}_k = \frac{\sum_{i=1}^n w_i ((\mathbf{X}_i - \boldsymbol{\mu}_k)(\mathbf{X}_i - \boldsymbol{\mu}_k)^\top)}{\sum_{i=1}^n w_i} \quad (6)$$

are calculated with the weighting factors $w_i = \text{qHPR}_k$ based on all available S_i for each hydrometeor class k in DP and DF space. Besic et al. (2016) and Trömel et al. (2023) apply a clustering algorithms to the multidimensional DP measurements and identified clusters are then assigned to specific hydrometeor classes using state-of-the-art HMC. Centroids $\boldsymbol{\mu}_k$ (in Trömel et al. (2023) also \mathbf{C}_k) are then calculated for these clusters. However, non-physical clusters in terms of precipitation microphysics
195 and strict boundaries between clustered data may arise, which have an impact on the calculations of centroids and covariance matrices in polarimetric space. Instead, the use of qHPR as weighting factors enables a more physical transition between the DP or DF variables for different hydrometeor classes. The multidimensional distribution functions p_k are calculated based on centroids $\boldsymbol{\mu}_k$ and covariances \mathbf{C}_k (Eq.5 and Eq.6) assuming a multivariate normal distribution

$$p_k(\mathbf{X}|\boldsymbol{\mu}_k, \mathbf{C}_k) = \Lambda \exp\left(-\frac{1}{2}(\mathbf{X} - \boldsymbol{\mu}_k)^\top \mathbf{C}_k^{-1}(\mathbf{X} - \boldsymbol{\mu}_k)\right) \quad (7)$$

200 with the transpose of a matrix $(\cdot)^\top$, the dimension d of the multivariate normal distribution and $\Lambda = 1/\sqrt{(2\pi)^d |\mathbf{C}_k|}$, where $|\cdot|$ denotes the determinant (Trömel et al., 2023). The multivariate normal distribution p_k replaces the exponential distribution used in Besic et al. (2018), allowing a more suitable elliptical (instead of only spherical) distributions of DP or DF variables for different hydrometeor classes. Besic et al. (2018) use the entropy to determine the shape of p_k , which is a purely statistical method. The inherent assumption is that the entropy and thus the mixing is highest exactly between two centroids. Trömel
205 et al. (2023) describe the shape of p_k with the observed distribution of the DP measurements in multidimensional space using the covariance matrices. Including now the qHPRs, as weighted factors, the centroids and covariance matrices are no longer restricted to the clusters with strict boundaries in polarimetric space, instead overlapping distributions are enabled.

The value of a $p_k(\boldsymbol{\mu}_k)$ equals 1 according for an unmixed observation (Besic et al., 2018), of only one specific hydrometeor class. Therefore, each $p_k(\mathbf{X})$ is normalized with $p_k(\boldsymbol{\mu}_k)$:

$$210 \quad \tilde{p}_k = \frac{p_k(\mathbf{X})}{p_k(\boldsymbol{\mu}_k)}. \quad (8)$$



Finally, HPRs for different hydrometeor classes k are estimated as follows:

$$\text{HPR}_k = \frac{W_k(T) \tilde{p}_k}{\sum_{k=1}^n W_k(T) \tilde{p}_k}. \quad (9)$$

The weighting functions $W_k(T)$ suppress HPR estimates of hydrometeor classes in unexpected temperature regions. $W_k(T)$ are derived from statistics of the relative occurrence of the different hydrometeor classes ($N(\text{HM}_k)$) in 2°C intervals between -80°C and 32°C . Resulting estimates of partitioning ratios for different hydrometeor classes k are referred to as HPR_k^{DP} and HPR_k^{DF} in DP and DF space, respectively.

4 Results

4.1 Multidimensional distribution function p_k in polarimetric and dual-frequency space

The \tilde{p}_k of the DP (Fig. 4) and DF variables (Fig. 5d, e and f), as well as of RT (Fig. 5a, b and c) for each hydrometeor class k are derived based on the training data set (Fig. 3, center) as described in Sect. 3 and represent the basis for the HMC_P . The hydrometeor classes are analyzed separately in the regions where they are most likely to occur, e.g. light rain (LR), moderate rain (MR), heavy rain (HR) and big drops (BD) in the liquid region, plates/dendrites (PD), ice crystals (IC) and snow (SN) in the solid region and wet snow (WS), graupel (GP), hail (HA) and rain/hail (RH) in the solid, liquid and melting region (mixed). Note that the figures mentioned above illustrate only two-dimensional representations of the multidimensional \tilde{p}_k , normalized according to Eq. 8 without weighting $W_k(T)$.

In DP space, the centroids of the hydrometeor classes LR, MR, HR (Fig. 4a, d and g) show in the Z_H - Z_{DR} and Z_H - K_{DP} plane an increasing Z_H with increasing Z_{DR} and K_{DP} respectively. With increasing Z_H ρ_{HV} is decreasing due to droplet growth and the associated increase in droplet flattening in liquid precipitation (Straka et al., 2000). The BD centroid shows an increased Z_{DR} compared to LR, MR and HR (Bechini and Chandrasekar, 2015). In DP space of the solid region (Fig. 4b, e and h), the centroids of PD differ from IC with respect to high Z_{DR} and K_{DP} values, which is in line with expected characteristics of ice particles especially in the dendritic growth layer (DGL). SN instead is characterized by reduced Z_{DR} and K_{DP} values but higher Z_H values, which is due to the increase in particle size and decrease in density during aggregation processes. As expected the \tilde{p}_k for PD show reduced ρ_{HV} values due to the diversity of ice particles in the DGL (Trömel et al., 2019; Thompson et al., 2014). With regard to the mixed hydrometeors (Fig. 4c, f and i) Z_H of the WS centroid is much lower compared to the ones of GP, RH and HA. The latter shows the highest Z_H . ρ_{HV} is the lowest in WS, followed by the two hail classes and then GP. HA and GP show lower Z_{DR} values compared to RH and WS due the impact of tumbling of HA and potentially conical shapes of GP (Straka et al., 2000).

In DF space (only $Z_{K_u}^m$ - $\text{DFR}_{K_u-K_a}^m$ space is shown) the centroids for liquid hydrometeors (Fig. 5d) show the typical behavior with increasing $\text{DFR}_{K_u-K_a}^m$ and increasing $Z_{K_u}^m$ due to increasing attenuation effects transitioning from LR to HR (Le and Chandrasekar, 2012). An even more pronounced increase in $\text{DFR}_{K_u-K_a}^m$ with rising $Z_{K_u}^m$ is observed for BD. This can be attributed to the additional influence of non-Rayleigh scattering effects when the droplet diameter exceeds 0.8 mm (Mroz et al.,

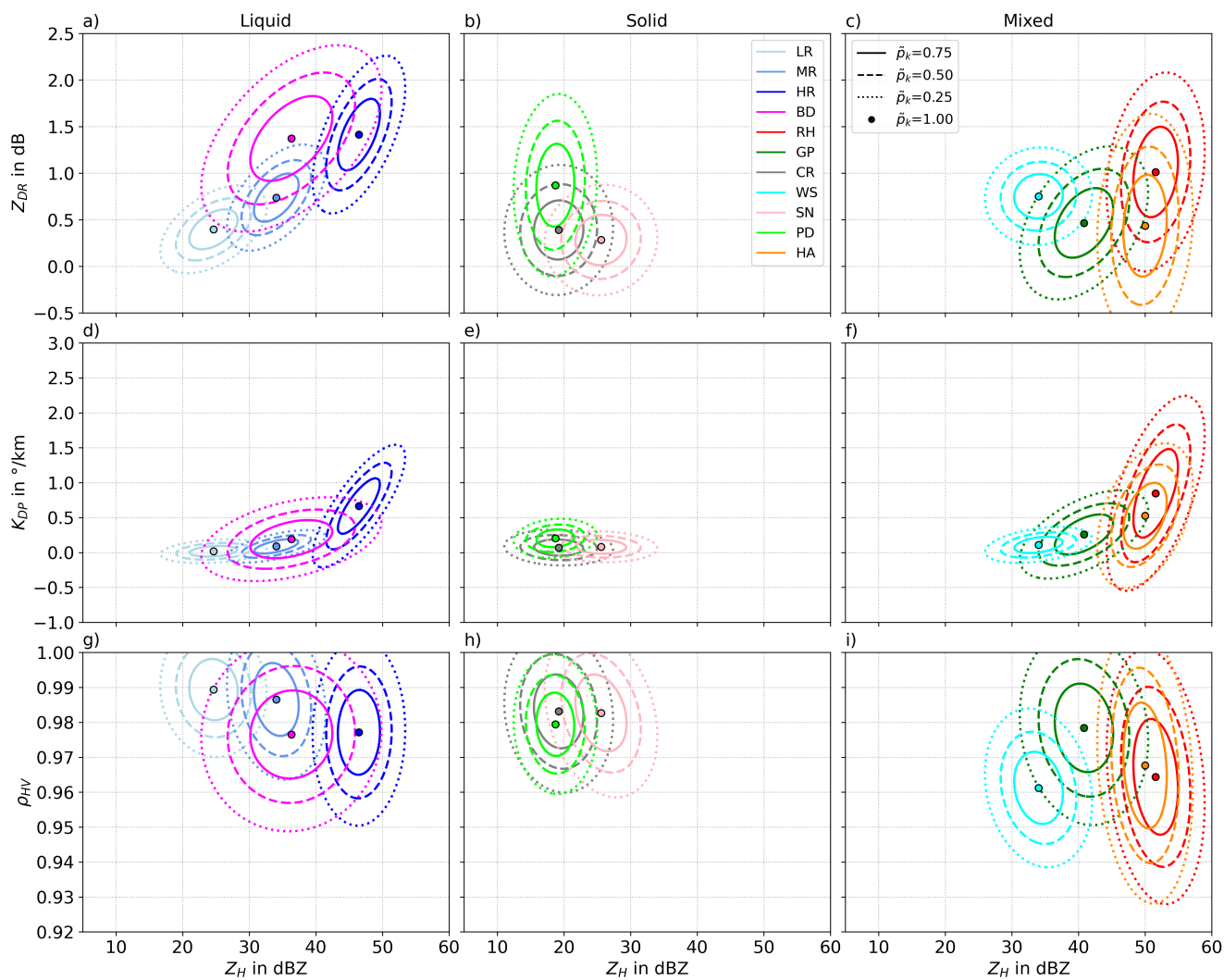


Figure 4. Normalized probability density functions \tilde{p}_k of the DP variables Z_H against Z_{DR} (a, b, and c), Z_H against K_{DP} (d, e and f) and Z_H against ρ_{HV} (g, h and i) for liquid hydrometeors (LR, MR, HR and BD, left column), solid hydrometeors (PD, SN, IC, center column) and mixed phase hydrometeors (RH, WS, GP and HA, right column). The different contour lines indicating the probabilities of the given \tilde{p}_k for the different hydrometeor classes.

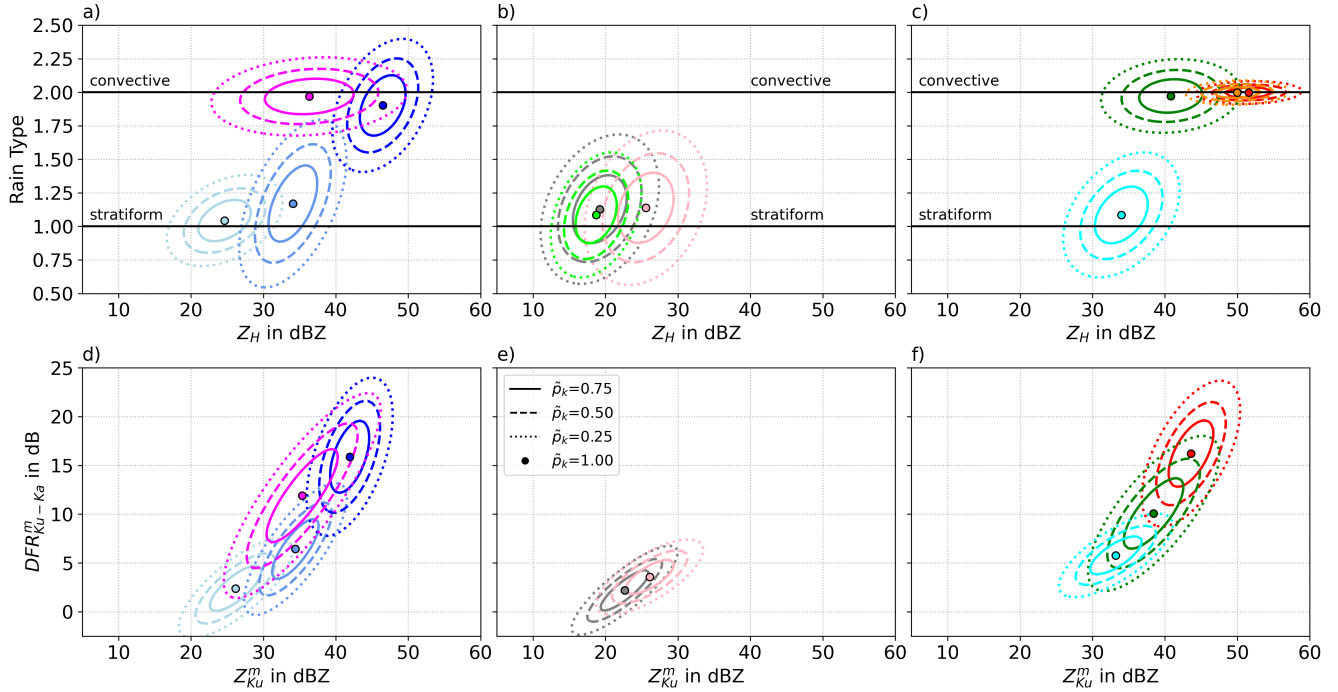


Figure 5. Normalized probability density function \tilde{p}_k of Z_H in relation to the RT (a, b and c) and the DF variables ($Z_{K_u}^m$ in relation to $DFR_{K_u-K_a}^m$, d, e and f), for liquid hydrometeors (LR, MR, HR and BD, left column), solid hydrometeors (PD, SN, IC, center column) and mixed phase hydrometeors (RH, WS, GP and HA, right column). The different contour lines indicating the probabilities of the given \tilde{p}_k for the different hydrometeor classes.

2024). $DFR_{K_u-K_a}^m$ show an increase for both IC and SN with increasing $Z_{K_u}^m$ due to the increasing impact of non-Rayleigh effects with increasing particle diameter (Fig. 5e). GP, WS and RH (Fig. 5f) show increased $DFR_{K_u-K_a}^m$ due to a combination of increased diameters, riming and attenuation effects (Le and Chandrasekar, 2021a; Tridon et al., 2019). Note that DF variables
 245 do not significantly differ between RH and HA nor between IC and PD (not shown). As a consequence the hydrometeor classes are merged to RH and IC.

BD, GP, RH and HA are mostly restricted to convective precipitation where HR has higher tendency to appear also in stratiform precipitation. LR, WS, SN, IC and PD are restricted to stratiform precipitation where WS, SN, IC and PD can occur with lower probabilities also in convection (Fig. 5a, b and c).

250 4.2 Evaluation with quasi hydrometeor partitioning ratios

In order to evaluate the DF- and DP-based HPR retrievals, HMC_P estimates (E) of the test dataset are compared to the qHPR serving as the reference (R), with the following statistical metrics:



$$\text{BIAS} = \sqrt{\frac{1}{N} \sum_{i=1}^N (E_i - R_i)} \quad , \quad (10)$$

$$\text{RMSE} = \sqrt{\frac{1}{N} \sum_{i=1}^N (E_i - R_i)^2} \text{ and} \quad (11)$$

$$255 \quad \text{CCP} = \frac{\sum_{i=1}^N (E_i - \bar{E}) (R_i - \bar{R})}{\sqrt{\sum_{i=1}^N (E_i - \bar{E})^2 \sum_{i=1}^N (R_i - \bar{R})^2}}. \quad (12)$$

\bar{R} and \bar{E} denote the mean values of R_i and E_i , respectively. A comparison between the qHPRs and HPRs based on the \overline{DF} and \overline{DP} variables results in high CCP for several hydrometeor classes. E.g., CCPs higher than 0.8, are achieved with the DP-based retrievals for LR, MR, HR, WS, IC and SN and with the DF-based retrievals for LR, MR, and SN (Fig. 6a, b, c, d, e, o, m, q and r). The lowest correlations occur with $\text{HPR}_{\text{BD}}^{\text{DP}}$ and $\text{HPR}_{\text{BD}}^{\text{DF}}$ (Fig. 6g and h) followed by $\text{HPR}_{\text{RH}}^{\text{DF}}$, $\text{HPR}_{\text{PD}}^{\text{DP}}$ and $\text{HPR}_{\text{IC}}^{\text{DF}}$ (Fig. 6j, n and t). The largest underestimations can be found in snow in both the DP and DF space, with a BIAS up to -5.15% (Fig. 6, q and r) followed $\text{HPR}_{\text{LR}}^{\text{DP}}$, $\text{HPR}_{\text{MR}}^{\text{DP}}$, $\text{HPR}_{\text{IC}}^{\text{DF}}$ and $\text{HPR}_{\text{WS}}^{\text{DF}}$ (Fig. 6, a, c, n and p). Pronounced HPR overestimation occurs for HR, GP for DF- and DP-based retrievals as well as for $\text{HPR}_{\text{BD}}^{\text{DP}}$ (Fig. 6e, f, g, k, and l). The comparison of hail HPRs shows a overestimation of $\text{HPR}_{\text{RH}}^{\text{DP}}$ and $\text{HPR}_{\text{HA}}^{\text{DP}}$ and small underestimation of $\text{HPR}_{\text{RH}}^{\text{DF}}$ (Fig. 6i, j and s). Note that qHPR estimated from the dominant hydrometeor classes may overestimate the actual partitioning ratios due to the disproportional impact of

265 hail on DP variables. As a consequence the biases in $\text{HPR}_{\text{RH}}^{\text{DP}}$ and $\text{HPR}_{\text{HA}}^{\text{DP}}$ may be even more pronounced than indicated by the qHPR-based evaluation. BIAS and RMSE values are small for the hail classes and BD, which can be attributed to their overall low HPR values.

In summary the DP-based retrievals outperform the ones based on DF in terms of CCP and RMSE, in most cases also with respect to the BIAS values. This can be attributed to the higher information content of DP compared to DF measurements, for

270 example, regarding the shape, orientation and homogeneity of the hydrometeors within the measurement volume. Except for the BD estimates, the retrievals for liquid hydrometeors in both DF- and DP-space, achieve a higher accuracy compared to the retrievals for the solid hydrometeor classes, reflecting the increased complexity and variability of DP and DF signals for solid and mixed hydrometeors.

4.3 Case study

275 To verify and illustrate the plausibility of the HMC_P retrievals, a GPM overflight is directly compared to the KDDC NEXRAD GR and a pseudo range height indicator (RHI) is generated along DPRs along-track scan (Fig. 7a, blue dashed and red solid lines). The DP (Fig. 7b, d, f and h) and DF (Fig. 7c, e and g) variables are exploited to derive and compare the HPR_k^{DP} (Fig. 9) and HPR_k^{DF} (Fig. 8) with the HMC_P .

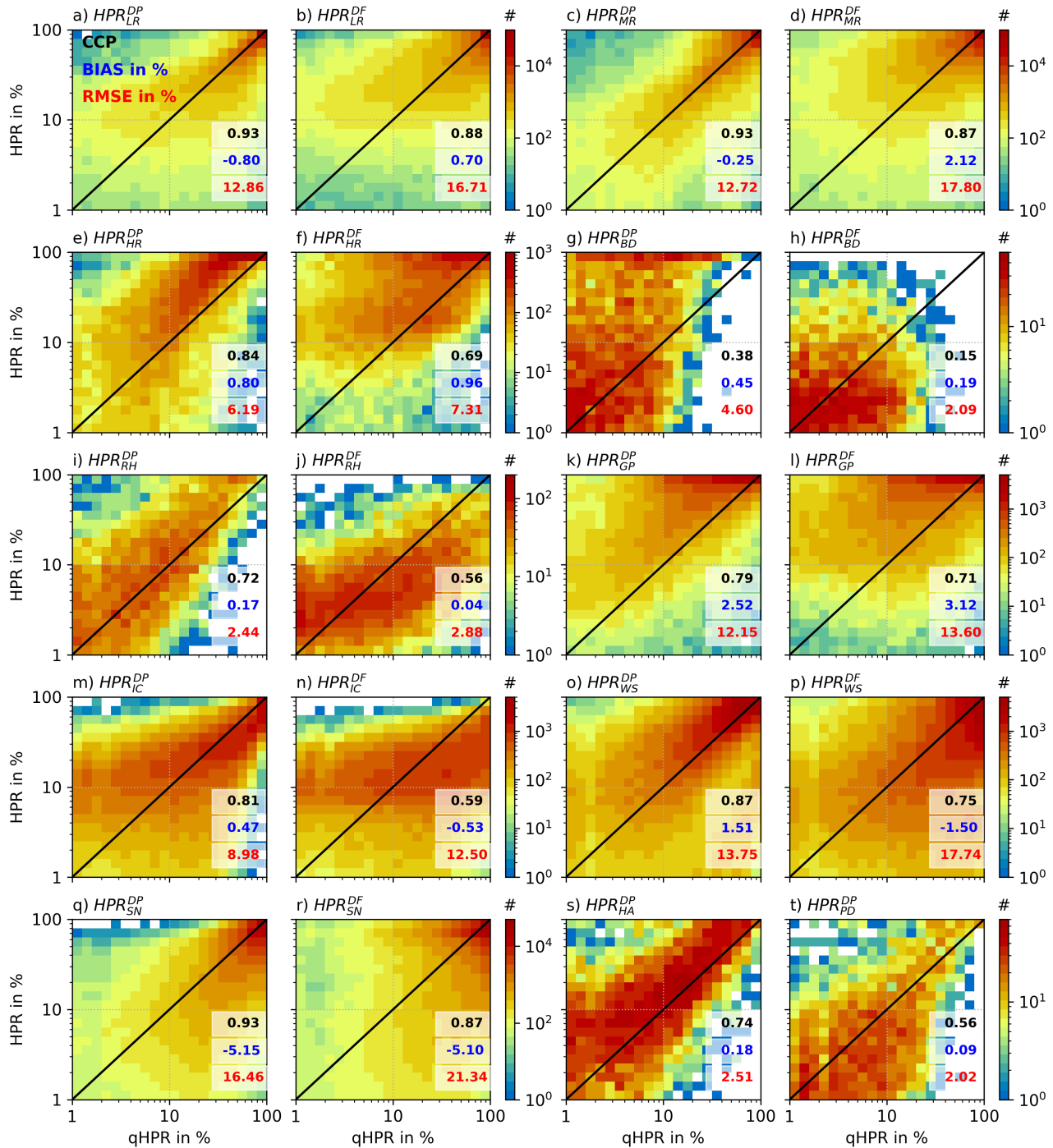


Figure 6. Two-dimensional histograms of the pairwise comparison HPR_k^{DF} and HPR_k^{DP} with $qHPR_k$ for the different hydrometeor classes. The CCP, BIAS and RMSE are in black, blue and red. The colors indicate the count of samples and the black solid line the 1:1 relationship.



A comparison of the GR and SR measurements (Fig. 7) reveals a slight discrepancy in the STH. While GR measurements
280 indicate a STH of approximately 15 km, SR indicate lower values due to the K_u PR and K_a PR sensitivity (Iguchi et al., 2010).
The precipitation event can be subdivided into a stratiform and convective region. According to the GR-based RT classification,
the convective area starts at a distance of 60 km from the GR, while the SR classification indicates that the convective area starts
at a distance of 50 km. This discrepancy is likely attributable to the presence of a bright band located approximately at 3.5 km
height characterized by increased Z_H , Z_{DR} , and reduced ρ_{HV} values, which is not properly identified by the DPR between
285 50 km and 60 km range and thus partly classified as a convective region. Additionally, the GR has identified further convective
areas up to a distance of 40 km, which may not be detected by SR due to their relatively small scale. The GR beams of
higher elevation angles are affected by differential attenuation in the ML resulting in negative Z_{DR} (Fig. 7d). At distances of
approximately 80 km and beyond, the measurements at low elevation angles are partially affected by non-uniform beam filling
(NBF), characterized by extreme high ϕ_{DP} (not shown) and low ρ_{HV} values (Ryzhkov and Zrnica, 2019). In the convective
290 region, the impact of attenuation on SR near surface measurements is significant, especially at K_a -band (not shown). The
signal partially drops below the 18 dBZ K_a -band threshold and is therefore excluded.

Until 50 km range, enhanced Z_{DR} and $DFR_{K_u-K_a}^m$ and moderate $Z_{K_u}^m$ and Z_H values result in corresponding increased
 HPR_{MR}^{DF} and HPR_{MR}^{DP} and low HPR_{LR}^{DF} and HPR_{LR}^{DP} (Fig. 8a, b and Fig. 9a, b). HPR_{BD}^{DF} appears with low ratios in the con-
vective region, whereas HPR_{BD}^{DP} does not show a clear signal. In a range between 10 km to 30 km the small-scale convective
295 regions are not detected by the DPR resulting in no HPR_{BD}^{DF} where small proportions of HPR_{BD}^{DP} are still estimated (Fig. 8d
and Fig. 9d). DP estimates effectively illustrate the transition from solid hydrometeors such as SN via WS to liquid hydrome-
teors such as LR, MR and HR. However, HPR_{WS}^{DF} do not match with DPRs bright-band detection where HPR_{WS}^{DP} is restricted
between $T_b = 0^\circ\text{C}$ and $T_t = 4^\circ\text{C}$ (Fig. 8h and Fig. 9h). HR is apparent in DP measurements within the ML, which is not the
case in the DF measurements (Fig. 8c and Fig. 9c).

300 Both DF and DP measurements allocate the transition zone from ice to snow retrievals at approximately 8 km altitude,
which corresponds to the height of the DGL (Fig. 8g, i and Fig. 9g, i) identified by increased K_{DP} values slightly above the
 -15°C isotherm (Fig. 7f). In the measurements obtained at ranges up to 20 km a decrease in K_{DP} and an increase in Z_H can
be identified below the -15°C isotherm (Fig. 7b, d and f) indicating aggregation processes (Trömel et al., 2019). This is
also supported by increasing $DFR_{K_u-K_a}^m$ measurements in the same region (Fig. 7g). Increased snow HPRs above the -15°C
305 isotherm may be connected to the underestimation of ice HPRs, as identified in Sect.4.2. The partial occurrence of HPR_{PD}^{DP} in
the DGL (Fig. 9j) is challenging to interpret due to the differential attenuation (Fig. 7d).

As expected rimed hydrometeors like GP, RH and HA, are primarily observed in convective regime. Due to the discrepancy
between RT classifications based on GR and SR measurements (f in Fig. 8 and Fig. 9) high HPR_{GP}^{DF} extend over a larger
region compared to HPR_{GP}^{DP} . Overall HPR of GP in DP and DF are significantly overestimated (compare Sect.4.2). A com-
310 parison of hail HPRs reveal a comparable vertical distribution up to an altitude of approximately 8 km. Note that HPR_{RH}^{DP} and
 HPR_{HA}^{DP} (Fig. 9e and k) have to be considered combined for a direct comparison with HPR_{RH}^{DF} (Fig. 7e). In regions with NBF,
the detection of hail has to be considered with caution due the similarity of the DP signals for NBF and hail. However, SR



partially confirms hail HPR in these areas. Due to the overall overestimation (underestimation) of hail HPRs in DP (DF) space, according estimates should be treated with caution.

315 5 Conclusions

This paper describes the most recent improvements of a more sophisticated hydrometeor classification (HMC) scheme to derive also hydrometeor partitioning ratios (HPRs). Such an algorithm has been first introduced by Besic et al. (2018) and enhanced in Trömel et al. (2023) (HMC_P). HMC_P is capable to derive HPRs from dual-polarization (DP) measurements (HMC_P^{DP}) of ground-based radars (GR) for each resolved volume. Combining GR DP observations from NEXRAD's WSR-88D S-band radars with space-borne radar (SR) dual-frequency (DF) observations, more precisely from the Dual-Frequency Precipitation Radar (DPR) onboard the Global Precipitation Measurement core satellite (GPM), allows to extend HMC_P for DF-based HPR estimates from SR observations (HMC_P^{DF}). Matching SR and GR observations, superobbed volumes containing a large number of GR pixels are generated and enable the estimation of quasi HPRs (qHPRs). These qHPRs represent the hydrometeor mixtures in superobbed volumes and are calculated with the identified dominant hydrometeor classes applying the modified standard HMC to the high-resolution GR measurements. The averaged DF and DP variables and qHPRs of the superobbed volumes are exploited for the training of HMC_P and also for the ensuing evaluation of HPR estimates. Such estimates are either based on DP (HPR_k^{DP}) or DF (HPR_k^{DF}) observations and compared with the qHPRs derived from averaged DF and DP variables, respectively. The derived \tilde{p}_k , which form the basis for the HMC_P , are in line with expected DP and DF observations for different hydrometeor classes (e.g. Straka et al., 2000; Bechini and Chandrasekar, 2015; Trömel et al., 2019; Thompson et al., 2014). A comparison between qHPRs and HPRs in DF (HPR_k^{DF}) and DP-space (HPR_k^{DP}) results in correlations higher than 0.7 for various hydrometeor classes. Lowest correlations are obtained for big drops in both DP- and DF-space with 0.38 and 0.15, respectively, followed by correlations for HPR_k^{DF} of ice with 0.59, dendrites/plates and rain/hail both with 0.56. HMC_P overestimates graupel and underestimates snow HPRs in DF and DP space. Hail HPRs are overestimated in DP and slightly underestimated in DF space. Overall, HPR estimates are more accurate in DP space than in DF space and perform best for liquid hydrometeors, except for big drops. DP observation provide additional information e.g. on the shape, orientation and homogeneity of the hydrometeors within the measurement volume compared to DF observations leads to more accurate derivations of HPR. Furthermore, HMC_P^{DP} and HMC_P^{DF} have been trained with DP data, also promoting a better performance in DP space. A case study revealed a high degree of agreement between GR- and SR-based estimates as well as a plausible vertical distribution of HPRs in the light of the DF and DP measurements.

340 Including additional information in the multidimensional observation vectors \mathbf{X}_i^{DF} and \mathbf{X}_i^{DP} could further improve the accuracy of the HPR estimates. E.g., for \mathbf{X}_i^{DF} vertical gradients of $Z_{K_u}^m$ or $DFR_{K_u-K_a}^m$ can be exploited. Battaglia et al. (2014), Mroz et al. (2018) and Le et al. (2016) demonstrated already their information content for the detection of hail and wet snow. Observations from other satellite devices, e.g. brightness temperatures from GPMs passive microwave radiometer utilized for hail (Mroz et al., 2017) or snow (Rysman et al., 2018, 2019) detection, could also be exploited to increase the information

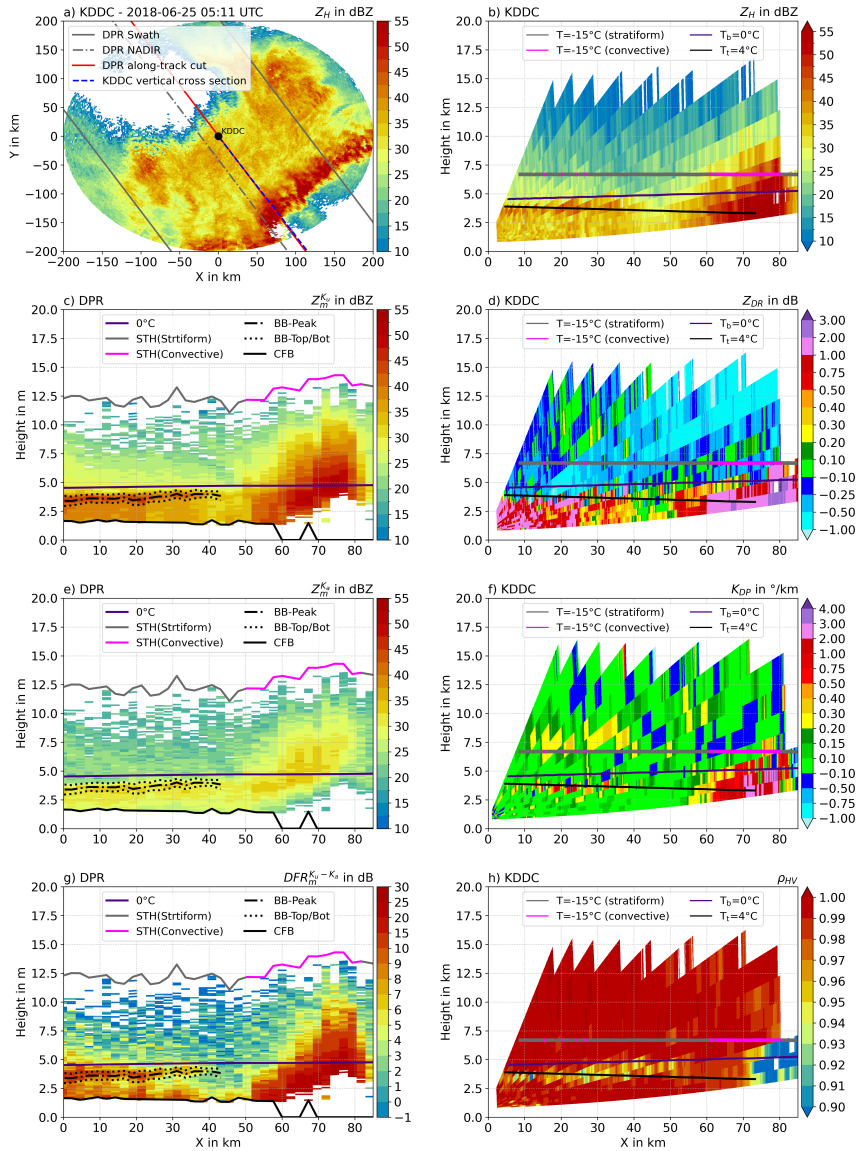


Figure 7. a) PPI of Z_H measured on 25 June 2018 at 05:11 UTC with KDDC and overpassed by GPM (orbit number 024557). Nadir along-track vertical cut of DPR-observed Z_{Ku}^m (c), Z_{Ka}^m (e) and DFR_{Ku-Ka}^m (g). Pseudo RHs of Z_H (b), Z_{DR} (d), K_{DP} (f), ρ_{HV} (h) along DPR's vertical cut. In panel a the gray lines indicate DPRs outer swath, the gray dashed line DPRs NADIR scan, the red line the along-track vertical cut and the blue line the location of the vertical cross section of the GR. In panels c, e and g the black line indicates the clutter free bottom, the indigo line the freezing level height (DPR), and the STH for convective (magenta) and for stratiform (cyan) SR-based RT. The dashed lines represent the bright band top and bottom. The bright band peak is illustrated as dash-dotted line. In panels b, d, f and h the black lines indicate the $T_t = 4^\circ C$ and the indigo lines the $T_b = 0^\circ C$ isotherms. The $T = -15^\circ C$ is indicated in gray/magenta for the GR-based stratiform/convective RT.

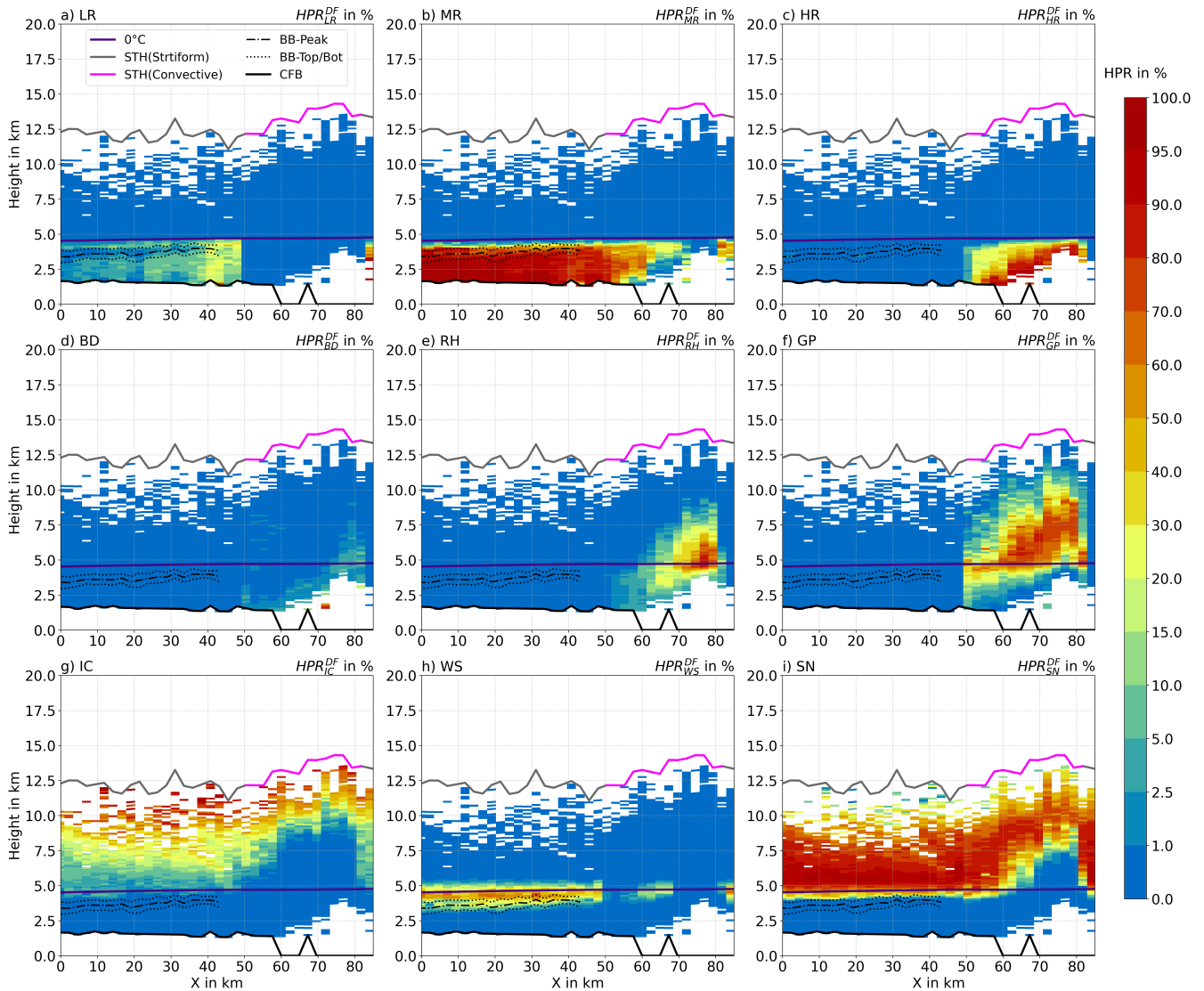


Figure 8. Estimated HPR_k^{DF} for different hydrometeor classes applying HMC_P to SR observations shown in Fig. 7. The black line indicates the clutter free bottom, the indigo line the freezing level height (DPR), and the STH for convective (magenta) and for stratiform (gray) SR-based RT. The dashed lines represent the bright band top and bottom. The bright band peak is illustrated as dash-dotted line.

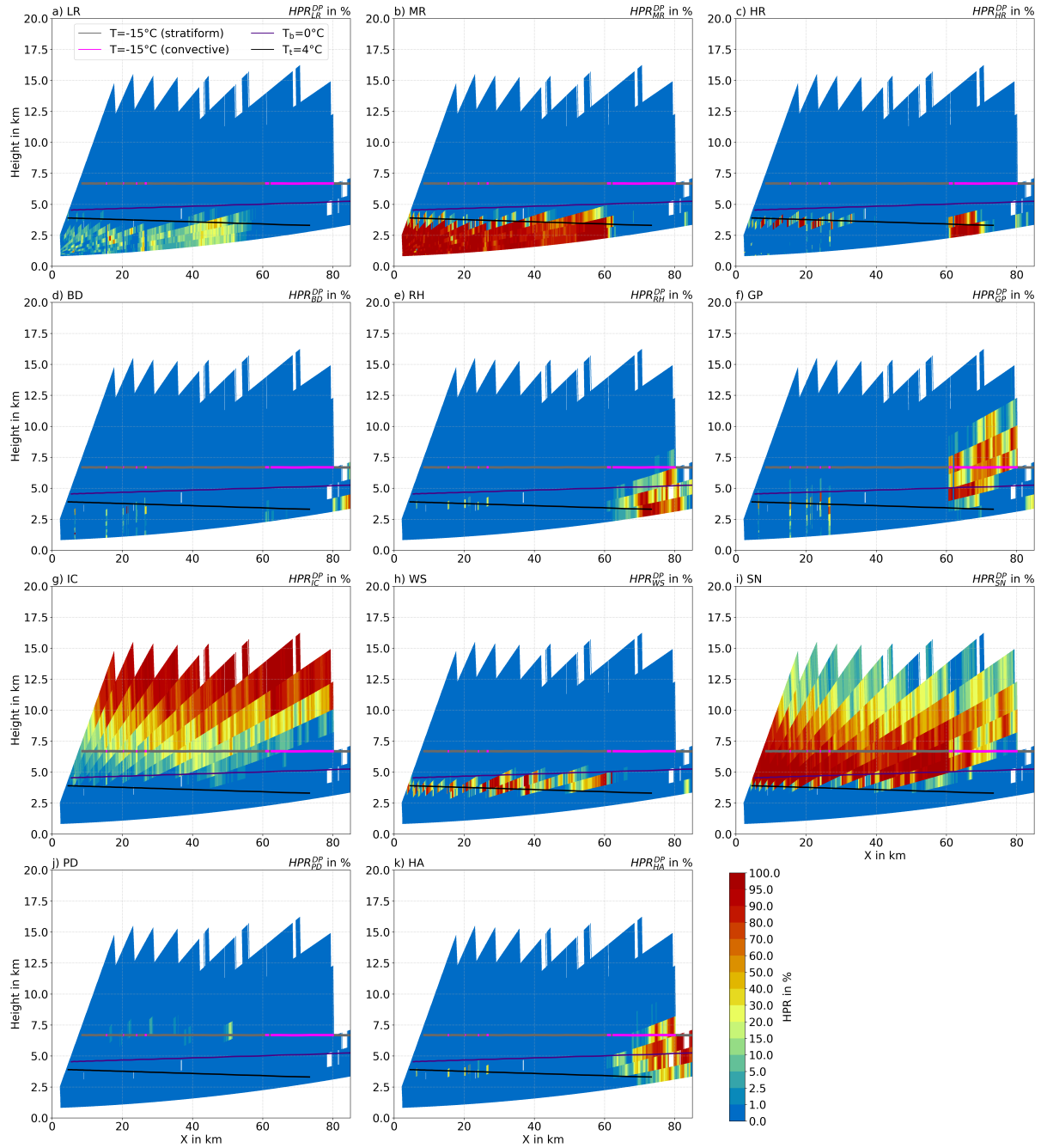


Figure 9. Estimated HPR_k^{DP} for different hydrometeor classes with HMC_P with GR observations shown in Fig. 7 The black lines indicate the $T_t = 4^\circ C$ and the indigo lines the $T_b = 0^\circ C$ isotherms. The $T_c = -15^\circ C$ is indicated in gray/magenta for the GR-based stratiform/-convective RT.



345 content. With respect to GR observations, the depolarization ratio, which has been shown to be valuable for riming detection (Blanke et al., 2024), might extend X_i^{DP} .

The retrievals introduced in this paper can be considered as valuable for different meteorological aspects. E.g., more accurate hydrometeor classifications can refine the calibration of GR with SR observations (Cao et al., 2013; Pejčic et al., 2022) by adapting the frequency transformation much more precisely to specific hydrometeor classes. Using HMC_P^{DP} , the GPM DPRs
350 area-wide measurements now provide precise information on hydrometeor distributions in areas without GR measurements. This allows e.g. to extend the evaluation of hydrometeor distributions in numerical weather prediction (NWP) models (Trömel et al., 2023) to the global scale. The assimilation of GR-based measurements and retrievals (Trömel et al., 2023; Reimann et al., 2023), but also of SR-based reflectivity measurements (Ikuta et al., 2021; Kotsuki et al., 2023) and rainfall estimates Li et al. (2020) in NWP has been shown to improve the accuracy of numerical precipitation prediction. Thus, the assimilation of DF-
355 and DP-based HPRs may further improve the representation of hydrometeors in NWP.

Code and data availability. Codes for the data processing and intermediate data products can be made available upon request. HMC_P is available at ω radlib. The GPM data can be downloaded following Iguchi and Meneghini (2021) and the quality-controlled ground radar data can be requested by NASA's GPM Ground Validation program (GPM-GV).

Appendix A: The standard Hydrometeor Classification to identify the dominant hydrometeor class

360 The membership functions (MSFs, Tab. A1) for the hydrometeor classes heavy rain (HR), big drops (BD), rain/hail (RH), wet snow (WS) and graupel (GP) are adapted from Park et al. (2009), whereas the rain class is subdivided into the light rain (LR) and moderate rain (MR) classes with a Z_H threshold of 28 dBZ (Tab. A1 LR and MR columns) following Straka et al. (2000). Furthermore, the Z_{DR} MSF for IC is extended to negative values and the Z_H MSF for SN and IC includes the snow ice switch-over between 15 dBZ and 20 dBZ (Tab. A1 SN and IC column) following Thompson et al. (2014).

365 PD is added as a new class combining the MSFs of plates and dendrites from Thompson et al. (2014). For this purpose, the MSFs of the two hydrometeor classes are superimposed and only the outer boundaries are considered (Tab. A1 PD column). The ρ_{HV} -MSF for IC are used also for PD. For HA, the polarimetric MSF from Dolan et al. (2013) are applied. In general the trapezoidal MSFs of HA and PD are tuned until they overlap as good as possible with the membership beta functions used in Dolan et al. (2013) and Thompson et al. (2014).

370 The temperature MSFs are designed to allow solid phase hydrometeors IC and SN only at temperatures below 0°C and liquid phase hydrometeors at temperatures above 0°C. WS and PD are restricted to temperature regimes with their highest probability of occurrence (von Terzi et al., 2022; Lundquist et al., 2008; Heymsfield et al., 2021) and hydrometeors such as RH, BD, HA and GP are allowed to exist in all regions (liquid, solid and mixed phase). BD are restricted up to -32.5°C assuming the 6.5°C/km lapse rate. This corresponds to findings of van Lier-Walqui et al. (2016) reporting updrafts reaching around 5 km



375 above the freezing level. GP MSF for temperature are set to the temperature interval between -50°C and 30°C , which is consistent with the boundaries for high density and low density graupel in Dolan et al. (2013).

Table A1. Values x_1 , x_2 , x_3 and x_4 of the used trapezoidal membership functions for Z_H , Z_{DR} , LK_{DP} , ρ_{HV} and T . f_1 , f_2 , f_3 , g_1 and g_2 can be found in Park et al. (2009) Eq.4 and Eq.5

	LR	MR	HR	BD	RH	GP	CR	DS	WS	PD	DH
$x_1(Z_H)$ in dBZ	5.0	23.0	40.0	20.0	45.0	25.0	0.0	15.0	25.0	-1.0	45.0
$x_2(Z_H)$ in dBZ	10.0	28.0	45.0	25.0	50.0	35.0	5.0	20.0	30.0	2.0	50.0
$x_3(Z_H)$ in dBZ	28.0	45.0	55.0	45.0	75.0	50.0	15.0	35.0	40.0	26.0	67.0
$x_4(Z_H)$ in dBZ	33.0	50.0	60.0	50.0	80.0	55.0	20.0	40.0	50.0	31.0	72.5
$x_1(Z_{DR})$ in dB	$f_1-0.3$	$f_1-0.3$	$f_1-0.3$	$f_2-0.3$	-0.3	-0.3	-1.0	-0.3	0.5	1.3	-0.5
$x_2(Z_{DR})$ in dB	f_1	f_1	f_1	f_2	0.0	0	-0.8	0.0	1.0	1.6	-0.25
$x_3(Z_{DR})$ in dB	f_2	f_2	f_2	f_3	f_1	f_1	3.0	0.3	2.0	8.4	0.50
$x_4(Z_{DR})$ in dB	$f_2+0.5$	$f_2+0.5$	$f_2+0.5$	f_3+1	$f_1+0.5$	$f_1+0.5$	3.3	0.6	3.0	9.2	0.75
$x_1(LK_{DP})$	g_1-1	g_1-1	g_1-1	g_1-1	-10.0	-30.0	-5.0	-30.0	-30.0	-30.0	-30.0
$x_2(LK_{DP})$	g_1	g_1	g_1	g_1	-4.0	-25.0	0.0	-25.0	-25.0	-13.0	-29.0
$x_3(LK_{DP})$	g_2	g_2	g_2	g_2	g_1	10.0	10.0	10.0	10.0	-3.0	4.8
$x_4(LK_{DP})$	g_2+1	g_2+1	g_2+1	g_2+1	g_1+1	20.0	15.0	20.0	20.0	2.15	7.0
$x_1(\rho_{HV})$	0.95	0.95	0.92	0.92	0.85	0.90	0.95	0.95	0.88	0.94	0.80
$x_2(\rho_{HV})$	0.97	0.97	0.95	0.95	0.90	0.97	0.98	0.98	0.92	0.97	0.91
$x_3(\rho_{HV})$	1.00	1.00	1.00	1.00	1.00	1.00	1.00	1.00	0.95	0.99	0.99
$x_4(\rho_{HV})$	1.01	1.01	1.01	1.01	1.01	1.01	1.01	1.01	0.985	1.00	1.00
$x_1(T)$ in $^{\circ}\text{C}$	0.0	0.0	0.0	-32.5	-90.0	-50.0	-90.0	-90.0	-2.0	-20.0	-90.0
$x_2(T)$ in $^{\circ}\text{C}$	1.0	1.0	1.0	-19.5	-50.0	-40.0	-80.0	-80.0	0.0	-17.5	-50.0
$x_3(T)$ in $^{\circ}\text{C}$	50.0	50.0	50.0	50.0	50.0	5.0	-2.0	-2.0	4.0	-12.5	0.0
$x_4(T)$ in $^{\circ}\text{C}$	55.0	55.0	55	55.0	55.0	30.0	0.0	0.0	6.0	-10.0	5.0

Author contributions. VP developed the methodology for this work, designed the manuscript, performed the coding, processed the data and carried out the visualization and analysis. KM_u supported the code for the VMM. ST and KM_r provided the scientific advice and support in the development of the text.

380 *Competing interests.* The authors state that they have no conflict of interest.



Acknowledgements. Velibor Pejčić's research was carried out partially in the framework of the priority programme SPP 2115 "Polarimetric Radar Observations meet Atmospheric Modelling (PROM)" within the project "Operation Hydrometeors" and the research project Near-Realtime Precipitation Estimation and Prediction (RealPEP). Work done by Kamil Mroz was performed under a contract with the National Centre for Earth Observation. We would also like to extend our gratitude to Jason Pippitt and Daniel Watters for providing and supporting us with the GPM GV GR data and also thank NASA/JAXA for providing the GPM DPR data. Furthermore, we would like to express our gratitude to Julian Steinheuer for his scientific support.

Financial support. This research was funded by the German Research Foundation (Deutsche Forschungsgemeinschaft, DFG; 320397309 and 408027387).



390 References

- Ackermann, L., Soderholm, J., Protat, A., Whitley, R., Ye, L., and Ridder, N.: Radar and environment-based hail damage estimates using machine learning, *Atmospheric Measurement Techniques Discussions*, 2023, 1–24, <https://doi.org/https://doi.org/10.5194/amt-17-407-2024>, 2023.
- Battaglia, A., Tanelli, S., Heymsfield, G. M., and Tian, L.: The dual wavelength ratio knee: A signature of multiple scattering in airborne
395 Ku–Ka observations, *Journal of Applied Meteorology and Climatology*, 53, 1790–1808, <https://doi.org/https://doi.org/10.1175/JAMC-D-13-0341.1>, 2014.
- Bech, J., Codina, B., Lorente, J., and Bebbington, D.: The sensitivity of single polarization weather radar beam blockage correction to variability in the vertical refractivity gradient, *Journal of Atmospheric and Oceanic Technology*, 20, 845–855, [https://doi.org/https://doi.org/10.1175/1520-0426\(2003\)020<0845:TSOSPW>2.0.CO;2](https://doi.org/https://doi.org/10.1175/1520-0426(2003)020<0845:TSOSPW>2.0.CO;2), 2003.
- 400 Bechini, R. and Chandrasekar, V.: A Semisupervised Robust Hydrometeor Classification Method for Dual-Polarization Radar Applications, *Journal of Atmospheric and Oceanic Technology*, 32, 22 – 47, <https://doi.org/https://doi.org/10.1175/JTECH-D-14-00097.1>, 2015.
- Besic, N., Figueras i Ventura, J., Grazioli, J., Gabella, M., Germann, U., and Berne, A.: Hydrometeor classification through statistical clustering of polarimetric radar measurements: A semi-supervised approach, *Atmospheric Measurement Techniques*, 9, 4425–4445, <https://doi.org/10.5194/amt-9-4425-2016>, 2016.
- 405 Besic, N., Gehring, J., Praz, C., Figueras i Ventura, J., Grazioli, J., Gabella, M., Germann, U., and Berne, A.: Unraveling hydrometeor mixtures in polarimetric radar measurements, *Atmospheric Measurement Techniques*, 11, 4847–4866, <https://doi.org/10.5194/amt-11-4847-2018>, 2018.
- Billault-Roux, A.-C., Ghiggi, G., Jaffaux, L., Martini, A., Viltard, N., and Berne, A.: Dual-frequency spectral radar retrieval of snowfall microphysics: a physics-driven deep-learning approach, *Atmospheric Measurement Techniques*, 16, 911–940, <https://doi.org/10.5194/amt-16-911-2023>, 2023.
- 410 Blanke, A., Gergely, M., and Trömel, S.: A new aggregation and riming discrimination algorithm based on polarimetric weather radars, *EGUsphere*, 2024, 1–28, <https://doi.org/10.5194/egusphere-2024-3336>, 2024.
- Cao, Q., Hong, Y., Qi, Y., Wen, Y., Zhang, J., Gourley, J. J., and Liao, L.: Empirical conversion of the vertical profile of reflectivity from Ku-band to S-band frequency, *Journal of Geophysical Research: Atmospheres*, 118, 1814–1825, <https://doi.org/https://agupubs.onlinelibrary.wiley.com/doi/full/10.1002/jgrd.50138>, 2013.
- 415 Crisologo, I. and Heistermann, M.: Using ground radar overlaps to verify the retrieval of calibration bias estimates from spaceborne platforms, *Atmospheric Measurement Techniques*, 13, 645–659, <https://doi.org/https://doi.org/10.5194/amt-13-645-2020>, 2020.
- Diekema, E. and Koornwinder, T. H.: Differentiation by integration using orthogonal polynomials, a survey, *Journal of Approximation Theory*, 164, 637–667, <https://doi.org/https://doi.org/10.1016/j.jat.2012.01.003>, 2012.
- 420 Dolan, B. and Rutledge, S. A.: A theory-based hydrometeor identification algorithm for X-band polarimetric radars, *Journal of Atmospheric and Oceanic Technology*, 26, 2071–2088, <https://doi.org/10.1175/2009JTECHA1208.1>, 2009.
- Dolan, B., Rutledge, S. A., Lim, S., Chandrasekar, V., and Thurai, M.: A robust C-band hydrometeor identification algorithm and application to a long-term polarimetric radar dataset, *Journal of Applied Meteorology and Climatology*, 52, 2162–2186, <https://doi.org/10.1175/JAMC-D-12-0275.1>, 2013.
- 425 Gehring, J., Oertel, A., Vignon, E., Jullien, N., Besic, N., and Berne, A.: Microphysics and dynamics of snowfall associated with a warm conveyor belt over Korea, *Atmospheric Chemistry and Physics*, 20, 7373–7392, <https://doi.org/10.5194/acp-20-7373-2020>, 2020.



- Gehring, J., Vignon, É., Billault-Roux, A.-C., Ferrone, A., Protat, A., Alexander, S. P., and Berne, A.: Orographic flow influence on precipitation during an atmospheric river event at Davis, Antarctica, *Journal of Geophysical Research: Atmospheres*, 127, e2021JD035210, <https://doi.org/10.1029/2021JD035210>, 2022.
- 430 Giangrande, S. E. and Ryzhkov, A. V.: Estimation of rainfall based on the results of polarimetric echo classification, *Journal of applied meteorology and climatology*, 47, 2445–2462, <https://doi.org/https://doi.org/10.1175/2008JAMC1753.1>, 2008.
- Grazioli, J., Tuia, D., and Berne, A.: Hydrometeor classification from polarimetric radar measurements: a clustering approach, *Atmospheric Measurement Techniques*, 8, 149–170, <https://doi.org/10.5194/amt-8-149-2015>, 2015.
- Heistermann, M., Jacobi, S., and Pfaff, T.: Technical Note: An open source library for processing weather radar data (wradlib), *Hydrology and Earth System Sciences*, 17, 863–871, <https://doi.org/10.5194/hess-17-863-2013>, 2013.
- 435 Heymsfield, A. J., Bansemer, A., Theis, A., and Schmitt, C.: Survival of snow in the melting layer: Relative humidity influence, *Journal of the Atmospheric Sciences*, 78, 1823–1845, <https://doi.org/https://doi.org/10.1175/JAS-D-20-0353.1>, 2021.
- Hou, A. Y., Kakar, R. K., Neeck, S., Azarbarzin, A. A., Kummerow, C. D., Kojima, M., Oki, R., Nakamura, K., and Iguchi, T.: The global precipitation measurement mission, *Bulletin of the American meteorological Society*, 95, 701–722, [https://doi.org/10.1175/BAMS-D-13-](https://doi.org/10.1175/BAMS-D-13-00164.1)
- 440 00164.1, 2014.
- Iguchi, T. and Meneghini, R.: GPM DPR Precipitation Profile L2A 1.5 hours 5 km V07, Greenbelt, MD, Goddard Earth Sciences Data and Information Services Center (GES DISC), Accessed: 2024, Goddard Earth Sciences Data and Information Services Center (GES DISC), <https://doi.org/https://doi.org/10.5067/GPM/DPR/GPM/2A/07>, 2021.
- Iguchi, T., Seto, S., Meneghini, R., Yoshida, N., Awaka, J., Le, M., Chandrasekar, V., and Kubota, T.: GPM/DPR level-2 algorithm theoretical basis document, NASA Goddard Space Flight Center, 2010.
- 445 Iguchi, T., Kawamoto, N., and Oki, R.: Detection of intense ice precipitation with GPM/DPR, *Journal of Atmospheric and Oceanic Technology*, 35, 491–502, <https://doi.org/https://doi.org/10.1175/JTECH-D-17-0120.1>, 2018.
- Ikuta, Y., Okamoto, K., and Kubota, T.: One-dimensional maximum-likelihood estimation for spaceborne precipitation radar data assimilation, *Quarterly Journal of the Royal Meteorological Society*, 147, 858–875, <https://doi.org/https://doi.org/10.1002/qj.3950>, 2021.
- 450 Jang, S., Lim, K.-S. S., Ko, J., Kim, K., Lee, G., Cho, S.-J., Ahn, K.-D., and Lee, Y.-H.: Revision of WDM7 microphysics scheme and evaluation for precipitating convection over the Korean peninsula, *Remote Sensing*, 13, 3860, <https://doi.org/10.3390/rs13193860>, 2021.
- Kotsuki, S., Terasaki, K., Satoh, M., and Miyoshi, T.: Ensemble-Based Data Assimilation of GPM DPR Reflectivity: Cloud Microphysics Parameter Estimation With the Nonhydrostatic Icosahedral Atmospheric Model (NICAM), *Journal of Geophysical Research: Atmospheres*, 128, e2022JD037447, <https://doi.org/https://doi.org/10.1029/2022JD037447>, 2023.
- 455 Kubota, T., Masaki, T., Kikuchi, G., Ito, M., Higashiawatoko, T., Kanemaru, K., Takahashi, N., Yamamoto, K., Furukawa, K., and Nio, T.: Evaluation of Effects on Dual-Frequency Precipitation Radar Observations Due to the Orbit Boost of the GPM Core Observatory, in: *IGARSS 2024-2024 IEEE International Geoscience and Remote Sensing Symposium*, pp. 709–712, IEEE, <https://doi.org/https://doi.org/10.1109/IGARSS53475.2024.10641066>, 2024.
- Le, M. and Chandrasekar, V.: Hydrometeor profile characterization method for dual-frequency precipitation radar onboard the GPM, *IEEE Transactions on Geoscience and Remote Sensing*, 51, 3648–3658, <https://doi.org/10.1109/TGRS.2012.2224352>, 2012.
- 460 Le, M. and Chandrasekar, V.: Graupel and hail identification algorithm for the dual-frequency precipitation radar (DPR) on the GPM core satellite, *Journal of the Meteorological Society of Japan. Ser. II*, 99, 49–65, <https://doi.org/https://doi.org/10.2151/jmsj.2021-003>, 2021a.
- Le, M. and Chandrasekar, V.: A new hail product for GPM DPR, in: *2021 IEEE International Geoscience and Remote Sensing Symposium IGARSS*, pp. 828–831, IEEE, <https://doi.org/https://doi.org/10.1109/IGARSS47720.2021.9553825>, 2021b.



- 465 Le, M., Chandrasekar, V., and Biswas, S.: Evaluation and validation of GPM dual-frequency classification module after launch, *Journal of Atmospheric and Oceanic Technology*, 33, 2699–2716, <https://doi.org/10.1175/JTECH-D-15-0253.1>, 2016.
- Le, M., Chandrasekar, V., and Biswas, S.: An algorithm to identify surface snowfall from GPM DPR observations, *IEEE Transactions on Geoscience and Remote Sensing*, 55, 4059–4071, <https://doi.org/https://doi.org/10.1109/TGRS.2017.2687420>, 2017.
- Li, X., Mecikalski, J. R., Srikishen, J., Zavodsky, B., and Petersen, W. A.: Assimilation of GPM rain rate products with GSI data as-
470 simulation system for heavy and light precipitation events, *Journal of Advances in Modeling Earth Systems*, 12, e2019MS001618, <https://doi.org/https://doi.org/10.1029/2019MS001618>, 2020.
- Liao, L. and Meneghini, R.: GPM DPR retrievals: Algorithm, evaluation, and validation, *Remote Sensing*, 14, 843, <https://doi.org/https://doi.org/10.3390/rs14040843>, 2022.
- Liu, Z., Ostrenga, D., Teng, W., and Kempler, S.: Tropical Rainfall Measuring Mission (TRMM) precipitation data and services for research
475 and applications, *Bulletin of the American Meteorological Society*, 93, 1317–1325, <https://doi.org/https://doi.org/10.1175/BAMS-D-11-00152.1>, 2012.
- Louf, V. and Protat, A.: Real-time monitoring of weather radar network calibration and antenna pointing, *Journal of Atmospheric and Oceanic Technology*, 40, 823–844, <https://doi.org/https://doi.org/10.1175/JTECH-D-22-0118.1>, 2023.
- Lukach, M., Dufton, D., Crosier, J., Hampton, J. M., Bennett, L., and Neely III, R. R.: Hydrometeor classification of quasi-vertical profiles
480 of polarimetric radar measurements using a top-down iterative hierarchical clustering method, *Atmospheric Measurement Techniques Discussions*, 2020, 1–33, <https://doi.org/10.5194/amt-2020-143>, 2020.
- Lundquist, J. D., Neiman, P. J., Martner, B., White, A. B., Gottas, D. J., and Ralph, F. M.: Rain versus snow in the Sierra Nevada, California: Comparing Doppler profiling radar and surface observations of melting level, *Journal of Hydrometeorology*, 9, 194–211, <https://doi.org/https://doi.org/10.1175/2007JHM853.1>, 2008.
- 485 Marzano, F. S., Scaranari, D., Montopoli, M., and Vulpiani, G.: Supervised classification and estimation of hydrometeors from C-band dual-polarized radars: A Bayesian approach, *IEEE transactions on Geoscience and Remote Sensing*, 46, 85–98, <https://doi.org/https://doi.org/10.1109/TGRS.2007.906476>, 2007.
- Mroz, K., Battaglia, A., Lang, T. J., Cecil, D. J., Tanelli, S., and Tridon, F.: Hail-detection algorithm for the GPM Core Observatory satellite sensors, *Journal of Applied Meteorology and Climatology*, 56, 1939–1957, <https://doi.org/https://doi.org/10.1175/JAMC-D-16-0368.1>,
490 2017.
- Mroz, K., Battaglia, A., Lang, T. J., Tanelli, S., and Sacco, G. F.: Global precipitation measuring dual-frequency precipitation radar observations of hailstorm vertical structure: Current capabilities and drawbacks, *Journal of Applied Meteorology and Climatology*, 57, 2161–2178, <https://doi.org/https://doi.org/10.1175/JAMC-D-18-0020.1>, 2018.
- Mroz, K., Battaglia, A., and Fridlind, A. M.: Enhancing consistency of microphysical properties of precipitation across
495 the melting layer in dual-frequency precipitation radar data, *Atmospheric Measurement Techniques*, 17, 1577–1597, <https://doi.org/https://doi.org/10.5194/amt-17-1577-2024>, 2024.
- Ortega, K. L., Krause, J. M., and Ryzhkov, A. V.: Polarimetric radar characteristics of melting hail. Part III: Validation of the algorithm for hail size discrimination, *Journal of Applied Meteorology and Climatology*, 55, 829–848, <https://doi.org/https://doi.org/10.1175/JAMC-D-15-0203.1>, 2016.
- 500 Park, H. S., Ryzhkov, A., Zrníć, D., and Kim, K.-E.: The hydrometeor classification algorithm for the polarimetric WSR-88D: Description and application to an MCS, *Weather and forecasting*, 24, 730–748, <https://doi.org/https://doi.org/10.1175/2008WAF2222205.1>, 2009.



- Pejcic, V., Soderholm, J., Mühlbauer, K., Louf, V., and Trömel, S.: Five years calibrated observations from the University of Bonn X-band weather radar (BoXPoI), *Scientific Data*, 9, 1–9, <https://doi.org/https://doi.org/10.1038/s41597-022-01656-0>, 2022.
- Pippitt, J. L., Marks, D. A., and Wolff, D. B.: Dual polarimetric quality control for NASA's Global Precipitation Measurement (GPM) Mission Ground Validation program. 36th Conf. on Radar Meteorology, Breckenridge, CO, Amer. Meteor. Soc, in: 36th AMS Conference on Radar Meteorology, Breckenridge, CO, September, vol. 16, p. 2013, <https://ams.confex.com/ams/36Radar/webprogram/Handout/Paper228522/36radarposter.pdf>, 2013.
- Planat, N., Gehring, J., Vignon, E., and Berne, A.: Identification of snowfall microphysical processes from Eulerian vertical gradients of polarimetric radar variables, *Atmospheric Measurement Techniques*, 14, 4543–4564, <https://doi.org/10.5194/amt-14-4543-2021>, 2021.
- 510 Protat, A., Louf, V., Soderholm, J., Brook, J., and Ponsonby, W.: Three-way calibration checks using ground-based, ship-based, and space-borne radars, *Atmospheric Measurement Techniques*, 15, 915–926, <https://doi.org/https://doi.org/10.5194/amt-15-915-2022>, 2022.
- Reimann, L., Simmer, C., and Trömel, S.: Assimilation of 3D polarimetric microphysical retrievals in a convective-scale NWP system, *Atmospheric Chemistry and Physics*, 23, 14 219–14 237, <https://doi.org/10.5194/acp-23-14219-2023>, 2023.
- Reuter, H. I., Nelson, A., and Jarvis, A.: An evaluation of void-filling interpolation methods for SRTM data, *International Journal of Geographical Information Science*, 21, 983–1008, <https://doi.org/https://doi.org/10.1080/13658810601169899>, 2007.
- 515 Ribaud, J.-F., Bousquet, O., Coquillat, S., Al-Sakka, H., Lambert, D., Ducrocq, V., and Fontaine, E.: Evaluation and application of hydrometeor classification algorithm outputs inferred from multi-frequency dual-polarimetric radar observations collected during HyMeX, *Quarterly Journal of the Royal Meteorological Society*, 142, 95–107, <https://doi.org/10.1002/qj.2589>, 2016.
- Ribaud, J.-F., Machado, L. A. T., and Biscaro, T.: X-band dual-polarization radar-based hydrometeor classification for Brazilian tropical precipitation systems, *Atmospheric Measurement Techniques*, 12, 811–837, <https://doi.org/10.5194/amt-12-811-2019>, 2019.
- 520 Rysman, J.-F., Panegrossi, G., Sanò, P., Marra, A. C., Dietrich, S., Milani, L., and Kulie, M. S.: SLALOM: An all-surface snow water path retrieval algorithm for the GPM Microwave Imager, *Remote Sensing*, 10, 1278, <https://doi.org/https://doi.org/10.3390/rs10081278>, 2018.
- Rysman, J.-F., Panegrossi, G., Sanò, P., Marra, A. C., Dietrich, S., Milani, L., Kulie, M. S., Casella, D., Camplani, A., Claud, C., et al.: Retrieving surface snowfall with the GPM microwave imager: A new module for the SLALOM algorithm, *Geophysical Research Letters*, 46, 13 593–13 601, <https://doi.org/https://doi.org/10.1029/2019GL084576>, 2019.
- 525 Ryzhkov, A. and Zrnica, D.: Precipitation and attenuation measurements at a 10-cm wavelength, *Journal of Applied Meteorology and Climatology*, 34, 2121–2134, [https://doi.org/10.1175/1520-0450\(1995\)034<2120:PAAMAA>2.0.CO;2](https://doi.org/10.1175/1520-0450(1995)034<2120:PAAMAA>2.0.CO;2), 1995.
- Ryzhkov, A. V. and Zrnica, D. S.: Radar polarimetry for weather observations, vol. 486, Springer, 2019.
- Ryzhkov, A. V., Kumjian, M. R., Ganson, S. M., and Zhang, P.: Polarimetric radar characteristics of melting hail. Part II: Practical implications, *Journal of Applied Meteorology and Climatology*, 52, 2871–2886, <https://doi.org/10.1175/JAMC-D-13-074.1>, 2013.
- 530 Sanchez-Rivas, D. and Rico-Ramirez, M. A.: Calibration of radar differential reflectivity using quasi-vertical profiles, *Atmospheric Measurement Techniques*, 15, 503–520, <https://doi.org/https://doi.org/10.5194/amt-15-503-2022>, 2022.
- Seiki, T.: Near-global three-dimensional hail signals detected by using GPM-DPR observations, *Journal of the Meteorological Society of Japan. Ser. II*, <https://doi.org/https://doi.org/10.2151/jmsj.2021-018>, 2021.
- 535 Shrestha, P., Mendrok, J., Pejcic, V., Trömel, S., Blahak, U., and Carlin, J. T.: Evaluation of the COSMO model (v5. 1) in polarimetric radar space–impact of uncertainties in model microphysics, retrievals and forward operators, *Geoscientific Model Development*, 15, 291–313, <https://doi.org/10.5194/gmd-15-291-2022>, 2022.



- Stephens, G. L., Vane, D. G., Boain, R. J., Mace, G. G., Sassen, K., Wang, Z., Illingworth, A. J., O’connor, E. J., Rossow, W. B., Durden, S. L., et al.: The CloudSat mission and the A-Train: A new dimension of space-based observations of clouds and precipitation, *Bulletin of the American Meteorological Society*, 83, 1771–1790, <https://doi.org/https://doi.org/10.1175/BAMS-83-12-1771>, 2002.
- 540 Straka, J. M., Zrnić, D. S., and Ryzhkov, A. V.: Bulk hydrometeor classification and quantification using polarimetric radar data: Synthesis of relations, *Journal of Applied Meteorology and Climatology*, 39, 1341–1372, 2000.
- Thompson, E. J., Rutledge, S. A., Dolan, B., Chandrasekar, V., and Cheong, B. L.: A dual-polarization radar hydrometeor classification algorithm for winter precipitation, *Journal of Atmospheric and Oceanic Technology*, 31, 1457–1481, [https://doi.org/10.1175/JTECH-D-](https://doi.org/10.1175/JTECH-D-13-00119.1)
- 545 13-00119.1, 2014.
- Tridon, F., Battaglia, A., Chase, R. J., Turk, F. J., Leinonen, J., Kneifel, S., Mroz, K., Finlon, J., Bansemer, A., Tanelli, S., et al.: The microphysics of stratiform precipitation during OLYMPEX: Compatibility between triple-frequency radar and airborne in situ observations, *Journal of Geophysical Research: Atmospheres*, 124, 8764–8792, <https://doi.org/10.1029/2018JD029858>, 2019.
- Trömel, S., Ryzhkov, A. V., Bick, T., Mühlbauer, K., and Simmer, C.: Towards nowcasting of winter precipitation: The Black Ice Event in
- 550 Berlin 2014, *Meteorologische Zeitschrift*, 26, 147–160, <https://doi.org/10.1127/metz/2016/0778>, 2017.
- Trömel, S., Simmer, C., Blahak, U., Blanke, A., Ewald, F., Frech, M., Gergely, M., Hagen, M., Hörnig, S., Janjic, T., et al.: Overview: Fusion of radar polarimetry and numerical atmospheric modelling towards an improved understanding of cloud and precipitation processes, *Atmospheric Chemistry and Physics Discussions*, 2021, 1–36, <https://doi.org/https://doi.org/10.5194/acp-21-17291-2021>, 2021.
- Trömel, S., Ryzhkov, A. V., Hickman, B., Mühlbauer, K., and Simmer, C.: Polarimetric Radar Variables in the Layers of Melting and Dendritic
- 555 Growth at X Band—Implications for a Nowcasting Strategy in Stratiform Rain, *Journal of Applied Meteorology and Climatology*, 58, 2497 – 2522, <https://doi.org/https://doi.org/10.1175/JAMC-D-19-0056.1>, 2019.
- Trömel, S., Blahak, U., Evaristo, R., Mendrok, J., Neef, L., Pejčić, V., Scharbach, T., Shrestha, P., and Simmer, C.: Fusion of radar polarimetry and atmospheric modeling, chap. Chapter 7, p. 293–344, https://doi.org/10.1049/SBRA557G_ch7, 2023.
- van Lier-Walqui, M., Fridlind, A. M., Ackerman, A. S., Collis, S., Helmus, J., MacGorman, D. R., North, K., Kollias, P., and Posselt, D. J.: On polarimetric radar signatures of deep convection for model evaluation: Columns of specific differential phase observed during MC3E,
- 560 *Monthly weather review*, 144, 737–758, <https://doi.org/https://doi.org/10.1175/MWR-D-15-0100.1>, 2016.
- Vignon, E., Besic, N., Jullien, N., Gehring, J., and Berne, A.: Microphysics of snowfall over coastal East Antarctica simulated by Polar WRF and observed by radar, *Journal of Geophysical Research: Atmospheres*, 124, 11 452–11 476, <https://doi.org/10.1029/2019JD031028>, 2019.
- 565 von Terzi, L., Dias Neto, J., Ori, D., Myagkov, A., and Kneifel, S.: Ice microphysical processes in the dendritic growth layer: a statistical analysis combining multi-frequency and polarimetric Doppler cloud radar observations, *Atmospheric Chemistry and Physics*, 22, 11 795–11 821, <https://doi.org/10.5194/acp-22-11795-2022>, 2022.
- Warren, R. A., Protat, A., Siems, S. T., Ramsay, H. A., Louf, V., Manton, M. J., and Kane, T. A.: Calibrating ground-based radars against TRMM and GPM, *Journal of Atmospheric and Oceanic Technology*, 35, 323–346, 2018.
- 570 Yang, J., Zhao, K., Zhang, G., Chen, G., Huang, H., and Chen, H.: A Bayesian hydrometeor classification algorithm for C-band polarimetric radar, *Remote Sensing*, 11, 1884, <https://doi.org/https://doi.org/10.3390/rs11161884>, 2019.
- Zrnić, D. S., Ryzhkov, A., Straka, J., Liu, Y., and Vivekanandan, J.: Testing a procedure for automatic classification of hydrometeor types, *Journal of Atmospheric and Oceanic Technology*, 18, 892–913, [https://doi.org/10.1175/1520-0426\(2001\)018<0892:TAPFAC>2.0.CO;2](https://doi.org/10.1175/1520-0426(2001)018<0892:TAPFAC>2.0.CO;2), 2001a.



- 575 Znić, D. S., Ryzhkov, A., Straka, J., Liu, Y., and Vivekanandan, J.: Testing a procedure for automatic classification of hydrometeor types, *Journal of Atmospheric and Oceanic Technology*, 18, 892–913, [https://doi.org/10.1175/1520-0426\(2001\)018<0892:TAPFAC>2.0.CO;2](https://doi.org/10.1175/1520-0426(2001)018<0892:TAPFAC>2.0.CO;2), 2001b.